"Structural and Multidisciplinary Optimization" manuscript No.
(will be inserted by the editor)

Topology optimization for blood flow considering a hemolysis model

Diego Hayashi Alonso [1] · **Emílio Carlos Nelli Silva** [1]

Received: date / Accepted: date

Abstract In the past years, topology optimization has been studied for designing fluid flow devices, such as channels, valves and pumps, and also considering non-Newtonian fluid flows, such as blood. When considering blood flow devices, it is important to quantify and minimize the blood damage (given mainly by hemolysis). However, up to now, in topology optimization, hemolysis has been minimized in an indirect manner, by considering shear stress (or even energy dissipation) as the objective function to indirectly minimize hemolysis. This approach may give a general idea of where hemolysis may or may not appear, but the actual distribution of hemolysis can not be easily correlated. Therefore, a more direct measure may be better to evaluate hemolysis. The direct way to measure hemolysis is by considering the hemolysis index, which is given from a differential equation model (a "hemolysis model"). In this work, the hemolysis index computed though a hemolysis model is included in the topology optimization formulation. In order to illustrate this approach, the design of a 2D swirl flow device, which is based on an axisymmetric fluid flow with or without rotation around an axis, is considered. One relevant example in the field of blood flow devices is the design of blood pumps, which has been previously considered in topology optimization with the aim of indirectly reducing hemolysis. More specifically in terms of pump design for 2D swirl flow, the design of a Tesla-type blood pump is considered. A Tesla-type pump is a bladeless fluid flow device, in which the boundary layer effect is used for pumping the fluid. This principle of operation may lead to a smaller induction of blood damage. Together with the hemolysis index, the topology optimization is formulated by considering the relative energy dissipation for indirectly maximizing efficiency. The fluid is modeled considering a non-Newtonian fluid model, and the fluid flow is solved with the finite element method. In order to model the solid material to block the fluid flow, the traditional formulation of fluid topology optimization is augmented with the "Brinkman-Forchheimer model". Also, an additional penalization is considered in the non-Newtonian viscosity. The optimization problem is solved with IPOPT (Interior Point Optimization algorithm).

Keywords Fluid flow topology optimization · Hemolysis model · Blood flow · Brinkman-Forchheimer model · Tesla-type pump · Finite element method

Diego Hayashi Alonso
E-mail: diego.alonso@usp.br
ORCID: https://orcid.org/0000-0002-6032-9989

Emílio Carlos Nelli Silva
E-mail: ecnsilva@usp.br
ORCID: http://orcid.org/0000-0003-1715-1713

[1] Department of Mechatronics and Mechanical Systems Engineering, Polytechnic School of the University of São Paulo, SP, Brazil

1 Introduction

When applied to fluid flow, the topology optimization method consists of distributing the solid and fluid materials over a given design domain. From the original work (Borrvall and Petersson, 2003), there have been applications to various types of fluid flow, such as the linear Stokes flow (Borrvall and Petersson, 2003), the porous Darcy-Stokes flow (Guest and Prévost, 2006; Wiker et al., 2007), the laminar Navier-Stokes flow (Evgrafov, 2004; Olesen et al., 2006), flows with slight compressibility (Evgrafov, 2006), flows of non-Newtonian fluids (Pingen and Maute, 2010; Hyun

Published article (Published (Online first): March 15th, 2021):
Alonso, D.H. & Silva, E.C.N. **Topology optimization for blood flow considering a hemolysis model**. Struct Multidisc Optim 63, 2101–2123 (2021).
https://doi.org/10.1007/s00158-020-02806-x

et al., 2014; Romero and Silva, 2017; Alonso et al., 2020), turbulent flows (Papoutsis-Kiachagias et al., 2011; Yoon, 2016; Dilgen et al., 2018; Yoon, 2020), thermal-fluid flows (Sato et al., 2018; Ramalingom et al., 2018), unsteady flows (Nørgaard et al., 2016) etc. Fluid flow devices have also been designed with the topology optimization method, such as valves (Song et al., 2009), mixers (Andreasen et al., 2009), rectifiers (Jensen et al., 2012), and centrifugal bladed pumps/turbines (Romero and Silva, 2014; Sá et al., 2018; Alonso et al., 2019). When considering non-Newtonian fluids, some designs that have already been performed are of centrifugal bladed blood pumps (Romero and Silva, 2017), roller-type blood viscous micropumps (Zhang et al., 2016), arterial by-pass grafts (Zhang and Liu, 2015; Hyun et al., 2014; Kian, 2017), aneurism implants (Jiang et al., 2017), and viscoelastic rectifier design (Jensen, 2013).

The way the topology optimization method distributes solid and fluid may be guided by different approaches, such as: the "pseudo-density approach" (Borrvall and Petersson, 2003), in which the design variable (called pseudo-density) is distributed for each node/cell of the design domain; the "level-set approach" (Duan et al., 2016; Zhou and Li, 2008), in which the solid material is delimited by a contour line of a sinuous 3D surface; and the "topological derivatives approach" (Sokolowski and Zochowski, 1999; Sá et al., 2016), which optimizes through perturbations around the solid portions of the design domain. In this work, the "pseudo-density approach" is used. The "pseudo-density approach" may be able to provide more rapid and robust convergence, weaker dependence with respect to the initial distribution of the design variable and deal with multiple constraints (Deng et al., 2013).

Hemolysis is the premature damage of RBCs (Red Blood Cells), in which the membranes of the RBCs suffer lysis (i.e., "breakdown"), releasing their hemoglobin content into the plasma. According to Garon and Farinas (2004), an excess of hemoglobin free in the plasma is toxic and may lead to renal failure. The main causes of hemolysis are high shear stresses and the exposure times to these stress levels (i.e., even if the shear stress is high, if the exposure time is a few milliseconds, the resulting hemolysis should be minimum) (Behbahani et al., 2009; Ghattas et al., 1995; Garon and Farinas, 2004). Contributions from other effects such as osmosis, chemical and thermal processes can be neglected (Apel et al., 2001).

One main example of a blood flow device that has to deal with hemolysis during its operation is a blood pump, which may be part of VADs (Ventricular Assist Devices). In VADs, the stress conditions may happen due to the mechanical interaction of the blood flow with the device (Garon and Farinas, 2004). According to (Behbahani et al., 2009), modern atraumatic designs can avoid RBC lysis, but sublethal damage to the RBCs should also be reduced for middle- and long-term blood pumps, since even minor hemolysis can raise the hemoglobin level of the blood, deteriorating the patient's condition and possibly leading to kidney dysfunction and multiple organ failure.

The optimization of blood pumps has been first delineated by Antaki et al. (1995) for CFD (Computational Fluid Dynamics), considering: the minimization of the shear stress for indirectly minimizing hemolysis (Behbahani et al., 2009); the minimization of energy dissipation for improving the efficiency; and the minimization of vorticity for reducing the flow recirculation. Romero and Silva (2017) considers a simplified version closer to the "real" hemolysis index, according to Montevecchi et al. (1995), for the topology optimization of centrifugal bladed blood pumps. No previous work in topology optimization has yet considered the computation of the "real" hemolysis index, which requires the solution of a differential equation from a hemolysis model.

There are essentially two approaches for evaluating hemolysis in blood flow, which are: the "power-law approach" (based on the Giersiepen-Wurzinger correlation (Giersiepen et al., 1990)), and the "threshold approach" (Goubergrits, 2006). Since the "threshold approach" (Lu et al., 2001) is an "all or nothing approach", which assumes that there is a critical shear stress magnitude value ("hemolytic threshold") before which hemolysis is 0%, and above which hemolysis is 100%, it is not adequate for estimating hemolysis. The "power-law approach" is based on the Giersiepen-Wurzinger correlation (Giersiepen et al., 1990) and serves as the basis for all other hemolysis models (Giersiepen et al., 1990; Bludszuweit, 1995; Taskin et al., 2012; Fraser et al., 2010; Zhang et al., 2011). Since this correlation is a scalar equation originally developed for a constant uniform shear stress, it is known to overestimate the hemolysis index De Wachter and Verdonck (2002). Thus, in order to numerically predict the hemolysis index under more generic conditions, differential equations based on the Giersiepen-Wurzinger correlation have been developed. These equations may be solved by either of two approaches (Taskin et al., 2012; Fraser et al., 2010): the Lagrangian approach, in which the integration follows the pathlines, and the Eulerian approach, in which the integration is performed in the entire computational domain. According to Pauli et al. (2013), the advantage of the Lagrangian approach is that it is easier to compute the residence time (interval of time in which the RBCs are inside the

device). However, near zero velocities and recirculation regions pose a computational problem for computing the pathlines necessary for the Lagrangian approach, and, due to the choice of pathlines, the entire flow field is not necessarily considered (Fraser et al., 2010). Therefore, the Eulerian approach seems to be more interesting for computing the hemolysis index (Fraser et al., 2010).

Various hemolysis models have been developed, which are mainly the "linear damage index" model (Garon and Farinas, 2004), the "asymptotically consistent damage index" model (Farinas et al., 2006), and the "mechanical dose infinitesimal damage index" model (Grigioni et al., 2005). There are other models, such as: "linear damage accumulation" (Mitoh et al., 2003; Yano et al., 2003), which is restricted to the Lagrangian approach for each RBC pathline (i.e., can not be represented in an Eulerian form), "Power law damage accumulation" (Song et al., 2003), which fails to reproduce the total damage under uniform shear stress (from the Giersiepen-Wurzinger correlation) (Grigioni et al., 2004, 2005) and portrays some undesirable dependency with respect to the time step (Taskin et al., 2012), "Power law damage accumulation based on damage curve" (Yeleswarapu et al., 1995), and "infinitesimal damage index" (Grigioni et al., 2004), which depends on the residence time of the RBCs (interval of time in which the RBCs are inside the device, which affects the shape distortion of RBCs).

While the "linear damage index" and "asymptotically consistent damage index" models require solving a single differential equation for obtaining the hemolysis index, the "mechanical dose infinitesimal damage index" model requires solving two equations: one for a "mechanical dose" of hemolysis, and another for the "hemolysis index". In particular, the "asymptotically consistent damage index" model is the "linear damage index" model with a correction for only nondestroyed RBCs to undergo hemolysis, which means that it is more suitable for evaluating hemolysis. Since both "asymptotically consistent damage index" model and "mechanical dose infinitesimal damage index" model should be acceptable for evaluating hemolysis (although the second one being more generic), and the "asymptotically consistent damage index" model requires solving a single differential equation, which is linear, the model selected in this work is the "asymptotically consistent damage index" model.

Since the main contributor to the blood behavior is the (time-independent) shear-thinning effect (Gijsen et al., 1999), the Carreau-Yasuda model (Gijsen et al., 1999; Pratumwal et al., 2017; Leondes, 2000) is chosen to model the blood flow.

In order to illustrate the inclusion of the hemolysis model in topology optimization, a 2D swirl flow device is considered (Alonso et al., 2018, 2019). This type of device assumes axisymmetric fluid flow with or without rotation around an axis. More specifically in terms of pump design, the design of a Tesla-type blood pump is considered in this work. The Tesla pump is a specific type of continuous flow pump which is bladeless, and the boundary layer effect is used for pumping the fluid. The basic principle of the Tesla pump is referred in this work as "*Tesla principle*", for simplicity. According to Dodsworth (2016), "*Tesla principle*"-based devices are less sensible to vibration-induced cavitation in comparison to conventional bladed pumps. Also, since there is no flow separation as in bladed pumps, the noise level should be small (Hasinger and Kehrt, 1963). The application of a Tesla-type pump to VADs (Yu, 2015) is of great interest, because, since it is a rotating pump of continuous and nonpulsatile flow, its use can reduce blood damage (hemolysis and thrombosis (Izraelev et al., 2009; Miller et al., 1993; Miller and Rainer, 1999)), which are the main limiting factors to the time of usage of VADs (Sastry et al., 2006). In comparison to bladed pumps (in which the movement of the blades may induce hemolysis), according to Yu (2015), the average shear stress induced by the flow, which is the main cause of hemolysis, is smaller. The idea of using a Tesla device as a blood pump was first examined by Dorman et al. (1966) and from then it has been studied by various other scientists (Hasinger and Kehrt, 1963; Izraelev et al., 2009; Rice, 1991). There are also patents that consider the use of a Tesla pump as a VAD, with straight disks (Gill et al., 2009) and curved disks (Kletschka and Rafferty, 1975; Rafferty and Kletschka, 1972, 1976). Also, there are some commercial Tesla pump devices with conical-shaped disks (BPX-80 BIO-Pump Plus (Medtronic®), CentriFlux BR-100 (Braile® Biomédica)).

Therefore, the main objective of this work is including a hemolysis model in the topology optimization for blood flow (non-Newtonian fluid flow). The objective functions of the optimization are: to minimize the relative energy dissipation considering the viscous, porous and inertial effects (Borrvall and Petersson, 2003; Alonso et al., 2019); and to minimize the blood damage from the value of the hemolysis index, considering its calculation computed from a hemolysis model. The 2D swirl fluid flow modeling is solved by using the finite element method. The material model is an augmented version of the traditional one presented by Borrvall and Petersson (2003), and considers an additional inertial effect ("Brinkman-Forchheimer model", which is adapted in order to match Borrvall

and Petersson (2003)'s material model specification. The design variable is considered to be nodal. The additional penalization scheme for the non-Newtonian viscosity (Hyun et al., 2014; Alonso et al., 2020) is also considered, enforcing the low shear stress behavior of the non-Newtonian viscosity of blood in the modeled solid material. The FEniCS platform is used for the implementation of the finite element method, the sensitivities are computed by the adjoint method (Farrell et al., 2013; Mitusch et al., 2019), the optimizer is IPOPT (Interior Point Optimization algorithm) (Wächter and Biegler, 2006), and MUMPS (Amestoy et al., 2001) is used for solving the linearized equations of the weak form of the problem during the execution of the Newton-Raphson method of the simulation.

This paper is organized as follows: in Section 2, the fluid flow model of the example (Tesla-type blood pump rotor) is briefly derived, and the non-Newtonian fluid model is presented; in Section 3, the weak formulation of the problem and the finite element modeling are presented; in Section 4, the hemolysis model is described; in Section 5, the topology optimization is stated by considering the Brinkman-Forchheimer model, and the hemolysis model; in Section 6, the numerical implementation is briefly described; in Section 7, numerical results are presented; and in Section 8, some conclusions are inferred.

2 Equilibrium equations

The fluid flow modeling is performed from the continuity and linear momentum (Navier-Stokes) equations, incompressible fluid and steady-state regime. It is presented by considering the design of a 2D swirl blood flow device (considered in this work as a Tesla-type blood pump). For 2D or 3D models, the main changes from the 2D swirl flow formulation are the different integration domains (such as $2\pi r d\Gamma$ becomes $d\Gamma$, and $2\pi r d\Omega$ becomes $d\Omega$) and the different definitions of the differential operators (cylindrical or Cartesian coordinates).

2.1 2D swirl flow model

By considering a rotating reference frame, the continuity and Navier-Stokes equations according to a porosity model are (Munson et al., 2009; White, 2009; Romero and Silva, 2014)

$$\nabla \bullet \boldsymbol{v} = 0 \tag{1}$$

$$\rho \nabla \boldsymbol{v} \bullet \boldsymbol{v} = \nabla \bullet \boldsymbol{T} + \rho \boldsymbol{f} - 2\rho(\boldsymbol{\omega} \wedge \boldsymbol{v}) - \rho \boldsymbol{\omega} \wedge (\boldsymbol{\omega} \wedge \boldsymbol{s}) + \boldsymbol{f}_r(\alpha) \tag{2}$$

where $\boldsymbol{v}$ is the velocity of the fluid with respect to the rotating reference frame, p is the pressure of the fluid, ρ is the density of the fluid, μ is the dynamic viscosity of the fluid, $\rho \boldsymbol{f}$ is the body force acting on the fluid per unit volume, $\boldsymbol{s}$ is position, $\wedge$ is used to denote cross product, $-2\rho(\boldsymbol{\omega} \wedge \boldsymbol{v})$ is the Coriolis force, $-\rho \boldsymbol{\omega} \wedge (\boldsymbol{\omega} \wedge \boldsymbol{s})$ is the centrifugal inertial force, $\boldsymbol{f}_r(\alpha)$ is the resistance force of the porous medium (which is considered in topology optimization in order to model a solid medium), α is the pseudo-density, whose values range from 0 (solid) to 1 (fluid) and is considered as the design variable of topology optimization, and $\boldsymbol{T}$ is the stress tensor defined by

$$\boldsymbol{T} = 2\mu \boldsymbol{\epsilon} - p\boldsymbol{I} \ , \ \boldsymbol{\epsilon} = \tfrac{1}{2}(\nabla \boldsymbol{v} + \nabla \boldsymbol{v}^T) \tag{3}$$

The 2D swirl flow model ("2D axisymmetric model with swirl") considers axisymmetrical flow and cylindrical coordinates (see Fig. 1). Therefore, the position and velocity are given by

$$\boldsymbol{s} = (r,\ 0,\ z) = r\boldsymbol{e}_r + z\boldsymbol{e}_z \tag{4}$$

$$\boldsymbol{v} = (v_r,\ v_\theta,\ v_z) = v_r\boldsymbol{e}_r + v_\theta\boldsymbol{e}_\theta + v_z\boldsymbol{e}_z \tag{5}$$

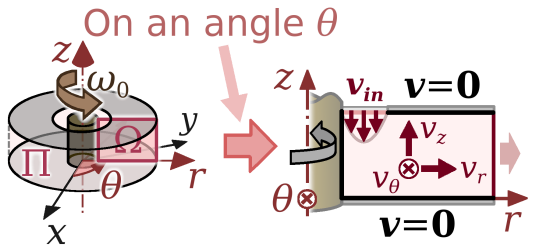

Fig. 1: Representation of the 2D swirl flow model for a Tesla-type blood pump device.

By considering axisymmetry, the derivatives of the state variables ($\boldsymbol{v}$ and p) in the θ direction become zero (i.e., $\frac{\partial v_r}{\partial \theta} = \frac{\partial v_\theta}{\partial \theta} = \frac{\partial v_z}{\partial \theta} = \frac{\partial p}{\partial \theta} = 0$). There is a development for equations for the 2D swirl flow model in Alonso et al. (2018).

2.2 Non-Newtonian fluid flow model

The behavior of the non-Newtonian fluid (blood) depends mainly on the (time-independent) shear-thinning effect (Gijsen et al., 1999), which may be modeled by

the Carreau-Yasuda model (Gijsen et al., 1999; Pratumwal et al., 2017; Leondes, 2000), which is given by (Cho and Kenssey, 1991; Bird et al., 1987)

$$\mu(\dot{\gamma}_{\mathrm{m}}) = \mu_{\infty} + (\mu_0 - \mu_{\infty})[1 + (\lambda\dot{\gamma}_{\mathrm{m}})^a]^{\frac{n-1}{a}} \tag{6}$$

where $\lambda = 1.902$ s is a time constant ("characteristic time"), $n = 0.22$ is an exponential factor, $a = 1.5$ is the Yasuda coefficient, $\mu_0 = 0.056$ Pa s is the maximum dynamic viscosity and $\mu_{\infty} = 0.00345$ Pa s is the minimum dynamic viscosity. The shear rate magnitude ("scalar shear rate") ($\dot{\gamma}_{\mathrm{m}}$) (Abraham et al., 2005) is given by (Lai et al., 2009; Arora et al., 2004, 2012).

$$\dot{\gamma}_{\mathrm{m}} = \sqrt{2\boldsymbol{\epsilon}\bullet\boldsymbol{\epsilon}} \tag{7}$$

where $\boldsymbol{\epsilon} = \frac{1}{2}(\nabla\boldsymbol{v} + \nabla\boldsymbol{v}^T)$ is the viscous stress deformation tensor and " $\bullet$ " is the inner product as defined in Gurtin (1981).

2.3 Boundary value problem

The computational domain is illustrated in Fig. 2. Then, the boundary value problem for the 2D swirl flow model can be stated as follows (Alonso et al., 2018, 2019).

$$\begin{aligned}
\rho\nabla\boldsymbol{v}\bullet\boldsymbol{v} = \nabla\bullet\boldsymbol{T}(\mu(\dot{\gamma}_{\mathrm{m}})) + \rho\boldsymbol{f} - 2\rho(\boldsymbol{\omega}\wedge\boldsymbol{v}) - \\
\rho\boldsymbol{\omega}\wedge(\boldsymbol{\omega}\wedge\boldsymbol{s}) + \boldsymbol{f}_r(\alpha) \quad &\text{in } \Omega \\
\nabla\bullet\boldsymbol{v} = 0 \quad &\text{in } \Omega \\
\boldsymbol{v} = \boldsymbol{v}_{in} \quad &\text{on } \Gamma_{\mathrm{in}} \\
\boldsymbol{v} = \boldsymbol{0} \quad &\text{on } \Gamma_{\mathrm{wall}} \\
\boldsymbol{T}(\mu(\dot{\gamma}_{\mathrm{m}}))\bullet\boldsymbol{n} = \boldsymbol{0} \quad &\text{on } \Gamma_{\mathrm{out}}
\end{aligned} \tag{8}$$

where the inside part of the computational domain (Ω), and the boundaries (Γ_{in}, Γ_{wall}, and Γ_{out}) are shown in Fig. 2. A fixed velocity profile is imposed on the inlet boundary (Γ_{in}), and the no-slip condition is set on the walls (Γ_{wall}). The outlet boundary (Γ_{out}) is set for a stress free condition (i.e., open to the atmosphere), where $\boldsymbol{n}$ is the normal unit vector to the boundaries (pointing outside) (in the 2D swirl flow model, $\boldsymbol{n} = (n_r,\ 0,\ n_z)$). $\boldsymbol{T}(\mu(\dot{\gamma}_{\mathrm{m}}))$ is the stress tensor ($\boldsymbol{T}$), which considers the non-Newtonian fluid model (eq. (6)).

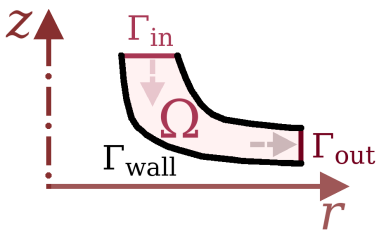

Fig. 2: Example of boundaries for the Tesla-type blood pump device.

3 Finite element method

The solution to the finite element method is performed from the weak formulation and finite elements described as follows.

3.1 Weak formulation

For the weak form, by considering the weighted-residual and Galerkin methods for the mixed (velocity-pressure) formulation, (Reddy and Gartling, 2010; Alonso et al., 2018)

$$R_c = \int_{\Omega} [\nabla\bullet\boldsymbol{v}] w_p r d\Omega \tag{9}$$

$$\begin{aligned}
R_m = \int_{\Omega} [\rho\nabla\boldsymbol{v}\bullet\boldsymbol{v} - \rho\boldsymbol{f} + 2\rho(\boldsymbol{\omega}\wedge\boldsymbol{v}) \\
+ \rho\boldsymbol{\omega}\wedge(\boldsymbol{\omega}\wedge\boldsymbol{s})]\bullet\boldsymbol{w}_v r d\Omega + \int_{\Omega} \boldsymbol{T}(\mu(\dot{\gamma}_{\mathrm{m}}))\bullet(\nabla\boldsymbol{w}_v) r d\Omega \\
- \oint_{\Gamma} (\boldsymbol{T}(\mu(\dot{\gamma}_{\mathrm{m}}))\bullet\boldsymbol{w}_v)\bullet\boldsymbol{n} r d\Gamma - \int_{\Omega} \boldsymbol{f}_r(\alpha)\bullet\boldsymbol{w}_v r d\Omega
\end{aligned} \tag{10}$$

where the subscript c is from the "continuity equation", the subscript m is from the "linear momentum equation" (i.e., the Navier-Stokes equations) and the test functions are w_p (for the pressure p), and $\boldsymbol{w}_v = \begin{bmatrix} w_{v,r} \\ w_{v,\theta} \\ w_{v,z} \end{bmatrix}$ (for the velocity $\boldsymbol{v}$). Since the integration domain ($2\pi r d\Omega$) features a multiplier that is constant (2π), this multiplier does not influence when solving the weak form, which means that eqs. (9) and (10) can be divided by 2π (Alonso et al., 2018, 2019).

From the two mutually independent test functions (w_p and $\boldsymbol{w}_v$), the eqs. (9) and (10) can be summed to a single equation

$$F = R_c + R_m = 0 \tag{11}$$

3.2 Finite element modeling

In order to achieve a numerically stable formulation (Brezzi and Fortin, 1991; Reddy and Gartling, 2010; Langtangen and Logg, 2016), Taylor-Hood elements are used for coupling the discretizations of pressure and velocity (see Fig. 3). The lowest degree Taylor-Hood elements consider 1st degree interpolation for pressure (P_1 element) and a 2nd degree interpolation for velocity (P_2 element). The pseudo-density (design variable) considers 1st degree interpolation (P_1 element).

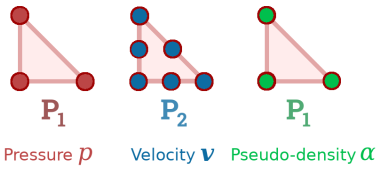

Fig. 3: Finite elements choice for the state variables (pressure and velocity), and the design variable (pseudo-density).

4 Hemolysis modeling

In order to model hemolysis, it is first necessary to define a measure for the shear stress magnitude ("scalar shear stress") acting over the RBCs, because it has an important role in hemolysis. There are two main approaches for this computation (Arora et al., 2004, 2012): stress-based and strain-based.

The first approach for computing the shear stress magnitude over the RBCs is the stress-based approach, which assumes that the RBCs deform immediately when under any shear stress. The shear stress magnitude is based on the shear stress tensor, which is the shear stress part of the stress tensor from eq. (3) (Alemu and Bluestein, 2007; Wu et al., 2005)

$$\boldsymbol{\tau} = \mu(\dot{\gamma}_{\mathrm{m}})(\nabla \boldsymbol{v} + \nabla \boldsymbol{v}^T) \tag{12}$$

Then, the shear stress magnitude (τ_{m}) may be computed through different methods and values. One common approach is by directly using the "instantaneous" shear stresses. This way, the resulting approach matches the shear rate magnitude described in eq. (7). Therefore, the shear stress magnitude may be given by (Tesch, 2013; Arora et al., 2004, 2012)

$$\tau_{\mathrm{m}} = \sqrt{2\boldsymbol{\tau} \bullet \boldsymbol{\tau}} \tag{13}$$

Other approaches that are also used for computing the shear stress magnitude (τ_{m}) assume it to be equal to, for example, a "von Mises stress"-like equation (Bludszuweit, 1995; Taskin et al., 2012; Fraser et al., 2010, 2011), a "Tresca stress"-like equation (Pinotti and Rosa, 1995; Garon and Farinas, 2004) or the second stress invariant (Pauli et al., 2013; Nam et al., 2011).

The second approach for computing the shear stress magnitude is the strain-based approach, which consists of considering the biophysical aspects of an RBC (shape distortion and relaxation of the viscoelastic membrane of the RBC) (Arora et al., 2004, 2012; Barthes-Biesel and Rallison, 1981) in determining the strain rate acting over the blood flow (and, therefore, the shear stress magnitude over the RBC) (Pauli et al., 2013). The main drawback of this method may be that it requires the solution of an additional tensorial equation, which may represent a high computational cost.

The main differences between these two approaches for computing the shear stress magnitude are that the stress-based approach assumes that the RBCs deform immediately, which is unrealistic under physiological conditions (Pauli et al., 2013), and does not consider the residence time (interval of time in which the RBCs are inside the device, which affects the shape distortion of the RBCs), which is normally small for blood pumps (Pauli et al., 2013). This means that the stress-based approach should overpredict blood damage (Pauli et al., 2013).

In this work, for simplicity and consistency with eq. (7), the shear stress magnitude for hemolysis is computed through the shear stress approach based on "instantaneous" shear stresses (eq. (13)).

4.1 Hemolysis index

Hemolysis may be evaluated by the hemolysis index. The hemolysis index (also called "blood damage index" in Grigioni et al. (2004)) is based on the quantity of hemoglobin (internal protein of RBCs responsible for transporting oxygen to the tissues) in the plasma, being given by (Fraser et al., 2010; Taskin et al., 2012)

$$I_{H,T} = \frac{\Delta \mathrm{Hb}_{\mathrm{pf}}}{\mathrm{Hb}} = \frac{\mathrm{Hb}_{\mathrm{pf,out}} - \mathrm{Hb}_{\mathrm{pf,in}}}{\mathrm{Hb}} \tag{14}$$

where $I_{H,T}$ is the hemolysis index (referred in this work as the "total" hemolysis index), $\Delta \mathrm{Hb}_{\mathrm{pf}} = \mathrm{Hb}_{\mathrm{pf,out}} - \mathrm{Hb}_{\mathrm{pf,in}}$ is the variation of the quantity of free hemoglobin in the plasma per volume of blood ("plasma free hemoglobin") (g/dL) and Hb is the quantity of hemoglobin per volume of blood (g/dL). For a healthy person, Hb = 1500 g/dL (Arora et al., 2006b,a).

While eq. (14) is essentially the difference between the outlet and the inlet hemoglobin, it is also possible

to define a "local" hemolysis index, which is distributed over the entire computational domain, as

$$I_H = \frac{\mathrm{Hb_{pf}}}{\mathrm{Hb}} \tag{15}$$

where I_H is the local hemolysis index and $\mathrm{Hb_{pf}}$ is the quantity of free hemoglobin in the plasma per volume of blood (g/dL).

The hemolysis index is sometimes weighted ("corrected") by the percentage of volume not occupied by RBCs in the total volume of blood ("plasma volume") (ASTM F1841-97, 1997; Garon and Farinas, 2004). This weighting is known to numerically underestimate the hemolysis (De Wachter and Verdonck, 2002; Garon and Farinas, 2004), and consists of multiplying eqs. (14) and (15) by $(1 - \mathrm{Ht})$, where $(1 - \mathrm{Ht})$ is the percentage of volume not occupied by RBCs in the total volume of blood, and Ht is the hematocrit (percentage of volume occupied by RBCs in the total volume of blood) (Billett, 1990). For a healthy person, Ht = 45 % (Arora et al., 2006b,a; Nam et al., 2011).

Since the local hemolysis index (I_H) varies with respect to each point of the flow, the value averaged by the flow rate can be used to define the total hemolysis index ($I_{H,T}$) Nam et al. (2011),

$$I_{H,T} = \frac{\int_{\Gamma_{\mathrm{out}}} I_H(\boldsymbol{v}\bullet\boldsymbol{n})2\pi r d\Gamma_{\mathrm{out}}}{\int_{\Gamma_{\mathrm{out}}} (\boldsymbol{v}\bullet\boldsymbol{n})2\pi r d\Gamma_{\mathrm{out}}} - \frac{\int_{\Gamma_{\mathrm{in}}} I_H(\boldsymbol{v}\bullet\boldsymbol{n})2\pi r d\Gamma_{\mathrm{in}}}{\int_{\Gamma_{\mathrm{in}}} (\boldsymbol{v}\bullet\boldsymbol{n})2\pi r d\Gamma_{\mathrm{in}}} \tag{16}$$

Since $(\boldsymbol{v}\bullet\boldsymbol{n})$ is different than zero only on inlets and outlets, and the flow rate that enters the fluid device is the same that exits it ($(\boldsymbol{v}\bullet\boldsymbol{n})|_{\mathrm{in}} = -(\boldsymbol{v}\bullet\boldsymbol{n})|_{\mathrm{out}}$) (i.e., the continuity equation is being respected), eq. (16) can also be written as:

$$I_{H,T} = \frac{\oint_\Gamma I_H(\boldsymbol{v}\bullet\boldsymbol{n})2\pi r d\Gamma}{Q} \tag{17}$$

where Q is the volumetric flow rate, which may be given from the outlet velocity or from the inlet velocity:

$$Q = \int_{\Gamma_{\mathrm{out}}} (\boldsymbol{v}\bullet\boldsymbol{n})2\pi r d\Gamma_{\mathrm{out}} = -\int_{\Gamma_{\mathrm{in}}} (\boldsymbol{v}\bullet\boldsymbol{n})2\pi r d\Gamma_{\mathrm{in}} \tag{18}$$

4.2 Asymptotically consistent damage index model

Since the "asymptotically consistent damage index" model consists of the "linear damage index" model with a correction, the "linear damage index" model is first briefly described as follows.

The "linear damage index" model assumes that the Giersiepen-Wurzinger correlation is valid for any fluid volume and completely describes the damage evolution of the blood flow (Garon and Farinas, 2004; Farinas et al., 2006; Taskin et al., 2012; Nam et al., 2011). In this case, the original equation of the Giersiepen-Wurzinger correlation is adapted to the differential form as follows (Garon and Farinas, 2004; Fraser et al., 2010), for each pathline,

$$\begin{aligned} \Delta I_H &= C_H \tau_{\mathrm{m}}^{\beta_s} \Delta t^{\beta_t} \\ \frac{(\Delta I_H)^{\frac{1}{\beta_t}}}{\Delta t} &= C_H^{\frac{1}{\beta_t}} \tau_{\mathrm{m}}^{\frac{\beta_s}{\beta_t}} \end{aligned} \tag{19}$$

where τ_{m} is the shear stress magnitude, Δt is here the time interval in the pathline of a single RBC, C_H is the proportionality factor for the hemolysis index, β_s is the exponent of the shear stress magnitude, and β_t is the exponent of the exposure time. The coefficients of the Giersiepen-Wurzinger correlation (C_H, β_s, β_t) are determined from regression of experimental data (Taskin et al., 2012). According to Zhang et al. (2011), the coefficients that were originally determined in Giersiepen et al. (1990) are overestimated because of the use of a mechanical seal in the experiments, and, therefore, Zhang et al. (2011) presents a new set of coefficients. The new set of coefficients consists of $C_H = 1.228\times10^{-5}$ $\mathrm{Pa}^{-\beta_s}\mathrm{s}^{-\beta_t}$, $\beta_s = 1.9918$, and $\beta_t = 0.6606$ (Zhang et al., 2011).

Then, it is assumed that $(\Delta I_H)^{\frac{1}{\beta_t}} \approx \Delta(I_H^{\frac{1}{\beta_t}})$, which is particularly true when $I_{H,\mathrm{in}} = 0$ in $\Delta I_H = I_{H,\mathrm{out}} - I_{H,\mathrm{in}}$ (* Notice that this assumption is not needed in the "mechanical dose infinitesimal damage index" model). By also considering a "linear damage index" (given by $I_{H,L} = I_H^{\frac{1}{\beta_t}}$), an infinitesimal time step ($\Delta t \to 0^+$) and τ_{m} being time-independent, the following equation is obtained:

$$\frac{DI_{H,L}}{Dt} = C_H^{\frac{1}{\beta_t}} \tau_{\mathrm{m}}^{\frac{\beta_s}{\beta_t}} \tag{20}$$

where the value of the local hemolysis index (I_H) is then recovered by considering $I_H = I_{H,L}^{\beta_t}$.

According to Nam et al. (2011), an additional diffusion term can also be included in eq. (20), but this term should not be significant in typical fluid flow devices.

According to Farinas et al. (2006), when the "linear damage index" model is under large shear stresses and/or exposure time, it may "generate" a hemolysis index larger than 1. This overestimates the hemolysis, since it would mean that already lysed RBCs continue being lysed (Farinas et al., 2006). In such case, it is needed to add a saturation effect to the hemolysis index computed by the "linear damage index" model. This saturation effect limits the maximum hemolysis index to 1 (i.e., 100% RBC destruction), removing nonphysical results from the validity range (Farinas et al., 2006).

Therefore, eq. (20) becomes the "asymptotically consistent damage index" model, given by(Farinas et al., 2006; Nam et al., 2011):

$$\frac{DI_{H,L}}{Dt} = C_H^{\frac{1}{\beta_t}} \tau_{\mathrm{m}}^{\frac{\beta_s}{\beta_t}} \underbrace{(1 - I_{H,L})}_{\substack{\text{Correction term} \\ \text{for nondestroyed} \\ \text{RBCs}}} \tag{21}$$

From the definition of the material derivative,

$$\frac{\partial I_{H,L}}{\partial t} + (\boldsymbol{v}_{\mathrm{abs}} \bullet \nabla) I_{H,L} = C_H^{\frac{1}{\beta_t}} \tau_{\mathrm{m}}^{\frac{\beta_s}{\beta_t}} (1 - I_{H,L}) \tag{22}$$

where $\boldsymbol{v}_{\mathrm{abs}}$ is the absolute velocity.

The weak form can be obtained by multiplying eq. (22) by the test function for the linear damage index ($w_{I_{H,L}}$), which would correspond to the weighted-residual and Galerkin methods. By also considering steady-state flow and dividing by 2π,

$$\int_\Omega \left[(\boldsymbol{v}_{\mathrm{abs}} \bullet \nabla) I_{H,L} - C_H^{\frac{1}{\beta_t}} \tau_{\mathrm{m}}^{\frac{\beta_s}{\beta_t}} (1 - I_{H,L}) \right] w_{I_{H,L}} r d\Omega = 0 \tag{23}$$

This approach is also referred as the FEM (Finite Element Method) approach. However, in the performed tests, this formulation resulted unstable for the solution of $I_{H,L}$ (i.e., the values resulted in a "checkerboard"-like distribution of extremely high positive and extremely low negative values). This is probably because, when the shear stress magnitude (τ_{m}) is small and the fluid velocity is also small ($\boldsymbol{v}_{\mathrm{abs}}$), there is a "singularity" in eq. (23) (i.e., "$0 \approx 0$"). Therefore, an alternative approach is considered. This alternative approach is based on the LSFEM (Least Squares Finite Element Method) formulation, as used in Nam et al. (2011) and Pauli et al. (2013). The LSFEM approach considers the minimization of $\int_\Omega R^2 r d\Omega$, where R is the residual of the differential equation and r is the radius necessary for the integration in the 2D swirl flow model. The minimization implies that the variational of $\int_\Omega R^2 r d\Omega$ be zero, which means that $\int_\Omega 2R\delta R r d\Omega = 0$ (or, when dividing by 2, $\int_\Omega R\delta R r d\Omega = 0$), where δR represents the variational of R. Therefore,

$$\int_\Omega \left[(\boldsymbol{v}_{\mathrm{abs}} \bullet \nabla) I_{H,L} - C_H^{\frac{1}{\beta_t}} \tau_{\mathrm{m}}^{\frac{\beta_s}{\beta_t}} (1 - I_{H,L}) \right] \left[(\boldsymbol{v}_{\mathrm{abs}} \bullet \nabla) w_{I_{H,L}} + C_H^{\frac{1}{\beta_t}} \tau_{\mathrm{m}}^{\frac{\beta_s}{\beta_t}} w_{I_{H,L}} \right] r d\Omega = 0 \tag{24}$$

In order to "soften" the "singularity" that may still be present near small shear stress magnitudes (τ_{m}) and small fluid velocities ($\boldsymbol{v}_{\mathrm{abs}}$) (i.e., "$0 \approx 0$"), eq. (24) is divided by $C_H^{\frac{1}{\beta_t}} \tau_{\mathrm{m}}^{\frac{\beta_s}{\beta_t}}$, resulting in:

$$\int_\Omega \left[\frac{(\boldsymbol{v}_{\mathrm{abs}} \bullet \nabla)}{C_H^{\frac{1}{\beta_t}} \tau_{\mathrm{m}}^{\frac{\beta_s}{\beta_t}}} I_{H,L} - (1 - I_{H,L}) \right] \left[(\boldsymbol{v}_{\mathrm{abs}} \bullet \nabla) w_{I_{H,L}} + C_H^{\frac{1}{\beta_t}} \tau_{\mathrm{m}}^{\frac{\beta_s}{\beta_t}} w_{I_{H,L}} \right] r d\Omega = 0 \tag{25}$$

By substituiting $\boldsymbol{v}_{\mathrm{abs}} = \boldsymbol{v} + \boldsymbol{\omega} \wedge \boldsymbol{s}$,

$$\int_\Omega \left[\frac{((\boldsymbol{v} + \boldsymbol{\omega} \wedge \boldsymbol{s}) \bullet \nabla)}{C_H^{\frac{1}{\beta_t}} \tau_{\mathrm{m}}^{\frac{\beta_s}{\beta_t}}} I_{H,L} - (1 - I_{H,L}) \right] \left[((\boldsymbol{v} + \boldsymbol{\omega} \wedge \boldsymbol{s}) \bullet \nabla) w_{I_{H,L}} + C_H^{\frac{1}{\beta_t}} \tau_{\mathrm{m}}^{\frac{\beta_s}{\beta_t}} w_{I_{H,L}} \right] r d\Omega = 0 \tag{26}$$

The formulation given by eq. (26) should be enough for evaluating the hemolysis index, and it also did not achieve negative values ("negative concentration problem"), as had been previously reported by Nam et al. (2011) in the formulation given by eq. (24). Therefore, there should be no need to consider a quadratic variable transformation, which is proposed in Nam et al. (2011) and requires the use of a non-linear solver (i.e., solving by using an iterative method, such as the Newton-Raphson method), with inherent convergence issues (Nam et al., 2011).

Since no boundary term appears in eq. (26), the only boundary condition that is imposed is a Dirichlet boundary condition on the inlet, which is considered in this work as zero inlet hemolysis ($I_H = 0 \implies I_{H,L} = 0$).

For the finite element modeling, the local hemolysis index (I_H) is considered with 1st degree interpolation (P_1 element) (see Fig. 4).

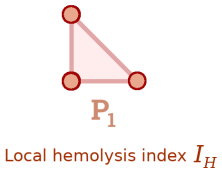

Fig. 4: Finite element choice for the local hemolysis index.

5 Formulation of the Topology optimization problem

5.1 Material model

The material model is augmented from the traditional one Borrvall and Petersson (2003), which includes only the Darcy term (Darcy, 1856; Brinkman, 1947) ("Brinkman model"), by considering an additional inertial effect ("Brinkman-Forchheimer model") (Forchheimer, 1901). This augmentation in the material model has been previously applied by Philippi and Jin (2015) in topology optimization, and is referred as the "complete porosity formulation", but can also be called "Brinkman-Forchheimer model" (or "Forchheimer model") (Huang and Ayoub, 2006; Alimohamadi et al., 2014). In order to match to the topology optimization formulation that was first presented by Borrvall and Petersson (2003), the "Brinkman-Forchheimer model" is briefly derived and formulated as follows.

In porous medium modeling (Geertsma, 1974), the Darcy's law (linear law) is valid to model porous material for low velocities (sufficiently low Reynolds numbers) (Lasseux and Valdés-Parada, 2017) and for single-phase flow (Kundu et al., 2016; Darcy, 1856; Wang et al., 2015). The Forchheimer's law (quadratic law) generalizes the formulation by including the Forchheimer correction ("non-Darcy flow behavior") to Darcy's law. The original formulation given by the Forchheimer's law comes from the pressure drop in a porous medium (Forchheimer, 1901; Geertsma, 1974; Bear, 2018; Joseph et al., 1982; Vafai, 2005).

$$-\nabla p = \underbrace{\frac{\mu(\dot{\gamma}_\mathrm{m})}{k_D}\boldsymbol{v}_\mathrm{mat}}_{\text{Darcy term}} + \underbrace{\beta_F \rho |\boldsymbol{v}_\mathrm{mat}| \boldsymbol{v}_\mathrm{mat}}_{\text{Forchheimer term}} \tag{27}$$

where k_D is the formation permeability, $\boldsymbol{v}_\mathrm{mat}$ is the velocity in relation to the porous material ($\boldsymbol{v}_\mathrm{mat} = (v_r,\ v_\theta - \omega_\mathrm{mat} r,\ v_z)$, where ω_mat is the rotation of the porous medium in relation to the reference frame), β_F is the coefficient of inertial flow resistance, and $|\boldsymbol{v}_\mathrm{mat}| = \sqrt{\boldsymbol{v}_\mathrm{mat} \bullet \boldsymbol{v}_\mathrm{mat}}$.

In eq. (27), according to Cimolin and Discacciati (2013), $\beta_F = \frac{C_F}{\sqrt{k_D}}$, where C_F is the "dimensionless form-drag constant" (Bear, 2018) (also called "Forchheimer constant" (Alimohamadi et al., 2014)). The porous medium of eq. (27) may then be given as a resistance force of the porous medium ($\boldsymbol{f}_r(\alpha)$ of eq. (2)). By also considering $\frac{\mu(\dot{\gamma}_\mathrm{m})}{k_D} \equiv \kappa(\alpha)$ and $\frac{\rho}{\sqrt{\mu(\dot{\gamma}_\mathrm{m})}} C_F \equiv k_\mathrm{inertia}$,

$$\boldsymbol{f}_r(\alpha) = \underbrace{-\kappa(\alpha)\boldsymbol{v}_\mathrm{mat}}_{\text{Darcy term}} \underbrace{-k_\mathrm{inertia}\sqrt{\kappa(\alpha)}|\boldsymbol{v}_\mathrm{mat}|\boldsymbol{v}_\mathrm{mat}}_{\text{Forchheimer term}} \tag{28}$$

where $k_\mathrm{inertia} = \frac{\rho}{\sqrt{\mu(\dot{\gamma}_\mathrm{m})}} C_F$ is the inertial resistance factor, and $\kappa(\alpha)$ is the inverse permeability ("absorption coefficient"). In this work, since the porous material is not being used to model a specific type of porous material, the Forchheimer constant C_F is assumed as the "universal" value $C_F = 0.55$ (Philippi and Jin, 2015; Ward, 1964).

In eq. (28), the resistance force of the porous medium is divided in two parts: the "Darcy term", which acts as a reduction of the size of the fluid path in the porous medium, and the "Forchheimer term", which deaccelerates the fluid due to the inertia of the porous medium particles.

The aim in fluid topology optimization is to reach a sufficiently discrete pseudo-density (α) distribution in the design domain (0 for solid, and 1 for fluid). Between the binary values (0 and 1), the transition is relaxed, allowing an intermediate porous medium ("gray", with pseudo-density values between 0 and 1 (real values)). Borrvall and Petersson (2003) suggests a convex interpolation function for the inverse permeability $\kappa(\alpha)$:

$$\kappa(\alpha) = \kappa_\mathrm{max} + (\kappa_\mathrm{min} - \kappa_\mathrm{max})\alpha \frac{1+q}{\alpha+q} \tag{29}$$

where the value of the inverse permeability ($\kappa(\alpha)$) can achieve values between a maximum value (κ_max) and a minimum value (κ_min), and has a convexity (relaxation) guided by the penalization parameter $q > 0$, where, when q is a large value, it leads to a less relaxed material model. It can be mentioned that it is also possible to use the Brinkman model instead of the Brinkman-Forchheimer model that is considered in this work, because, when considering a completely discrete topology (0 or 1) and a sufficiently high κ_max value, both models are able to block the fluid flow.

5.2 Material model for the non-Newtonian viscosity

An additional material model is considered for the non-Newtonian viscosity (eq. (6)), in the form of a penalization scheme (refered in this work as "non-Newtonian penalization"). It serves so as to enhance the behavior of the shear rate magnitude ($\dot{\gamma}_\mathrm{m}$) to be near zero inside a modeled solid material ($\alpha = 0$) (due to the fluid velocity being minimum). Therefore, the behavior of the non-Newtonian viscosity achieving its highest value inside the modeled solid material ($\mu(\dot{\gamma}_\mathrm{m}) \approx \mu_0$) is enhanced. This penalization scheme has already been applied to 2D flow topology optimization (Hyun et al., 2014) and 2D swirl flow topology optimization (Alonso et al., 2020), and is given by

$$\mu(\alpha, \dot{\gamma}_\mathrm{m}) = \mu_0 + (\mu(\dot{\gamma}_\mathrm{m}) - \mu_0)\alpha \frac{1+q}{\alpha+q} \tag{30}$$

where the viscosity value in the solid is the maximum dynamic viscosity (μ_0) and the viscosity value in the fluid is given as $\mu(\dot{\gamma}_\mathrm{m})$ (from eq. (6)). The penalization parameter ($q > 0$) assumes the same value used in eq. (29).

By considering eq. (30), $\mu(\alpha, \dot{\gamma}_\mathrm{m})$ is used in the place of $\mu(\dot{\gamma}_\mathrm{m})$ in the equations of the previous Sections.

5.3 Topology optimization problem

The topology optimization problem is formulated as:

$$\begin{aligned}
&\underset{\alpha}{\textbf{min}}\ J(p(\alpha), \boldsymbol{v}(\alpha), \alpha, I_H(p(\alpha), \boldsymbol{v}(\alpha), \alpha)) \\
&\textbf{such that} \\
&\quad \text{Fluid volume constraint: } \int_{\Omega_\alpha} \alpha(2\pi r d\Omega_\alpha) \leqslant f V_0 \\
&\quad \text{Box constraint of } \alpha\text{: } 0 \leqslant \alpha \leqslant 1
\end{aligned} \tag{31}$$

where f is the specified maximum fluid volume fraction, the volume of the design domain (represented as Ω_α) is given as $V_0 = \int_{\Omega_\alpha} 2\pi r d\Omega_\alpha$, $J(p(\alpha), \boldsymbol{v}(\alpha), \alpha, I_H(p(\alpha), \boldsymbol{v}(\alpha), \alpha))$ is the multi-objective function, $p(\alpha)$ and $\boldsymbol{v}(\alpha)$ are the pressure and velocity obtained by solving the boundary value problem (eq. (8)), which have an indirect dependency with the design variable α, and $I_H(p(\alpha), \boldsymbol{v}(\alpha), \alpha)$ is computed from eq. (26). In this work, the design domain is chosen as the entire computational domain ($\Omega_\alpha = \Omega$).

5.4 Multi-objective function

There are two objective functions defined in this work: the relative energy dissipation (for maximizing the efficiency) and the hemolysis index (for minimizing blood damage):

The relative energy dissipation is based on the energy dissipation objective function defined in Borrvall and Petersson (2003), also considering inertial effects, as defined in Alonso et al. (2019) for a rotating reference frame. The relative energy dissipation is closely related to the pressure increment in Stokes flow (Borrvall and Petersson, 2003), and to the pressure head in Navier-Stokes flow. By assuming zero external body forces,

$$\begin{aligned}
\Phi_\mathrm{rel} = &\int_\Omega \left[\frac{1}{2}\mu(\nabla \boldsymbol{v} + \nabla \boldsymbol{v}^T)\bullet(\nabla \boldsymbol{v} + \nabla \boldsymbol{v}^T)\right] 2\pi r d\Omega \\
&- \int_\Omega \boldsymbol{f}_r(\alpha)\bullet\boldsymbol{v} 2\pi r d\Omega \\
&+ \int_\Omega (2\rho(\boldsymbol{\omega}\wedge\boldsymbol{v}) + \rho\boldsymbol{\omega}\wedge(\boldsymbol{\omega}\wedge\boldsymbol{s}))\bullet\boldsymbol{v} 2\pi r d\Omega
\end{aligned} \tag{32}$$

In eq. (32), considering that the rotation vector is given by $\boldsymbol{\omega} = \omega_0 \boldsymbol{e}_z$ and considering eq. (4), the Coriolis term $(2\rho(\boldsymbol{\omega}\wedge\boldsymbol{v})\bullet\boldsymbol{v})$ becomes zero.

The total hemolysis index is given from eq. (16) or eq. (17), and computed from the weak form of the "asymptotically consistent damage index" model given in eq. (26).

A multi-objective function is defined to accomodate the two previously defined objective functions. Since the measurement units and magnitudes of the objective functions are different (the relative energy dissipation is given with power units (W), while the total hemolysis index is dimensionless), it is possible that the objective function magnitudes and sensitivities significantly vary from one another. In order to reduce this possible disparity and possible predominance of one objective function over the other during the optimization process, the following multi-objective function is used, which is based on the initial ratio between the objective function values,

$$J = w_\Phi \Phi_\mathrm{rel} + w_H \left(\frac{\Phi_{\mathrm{rel},0}}{I_{H,T,0}}\right) I_{H,T} \tag{33}$$

$$\frac{dJ}{d\alpha} = w_\Phi \frac{d\Phi_\mathrm{rel}}{d\alpha} + w_H \left(\frac{\Phi_{\mathrm{rel},0}}{I_{H,T,0}}\right) \frac{dI_{H,T}}{d\alpha} \tag{34}$$

where the weights w_Φ and w_H are constants ($w_\Phi + w_H = 1$), and $\Phi_{\mathrm{rel},0}$ and $I_{H,T,0}$ are the values of the objective functions before starting the IPOPT algorithm.

5.5 Sensitivity analysis

The solution of the hemolysis model needs to be considered in the sensitivity. By first applying the chain rule of derivatives,

$$\frac{dJ}{d\alpha} = \frac{\partial J}{\partial(p, \boldsymbol{v})}\frac{d(p, \boldsymbol{v})}{d\alpha} + \frac{\partial J}{\partial \alpha}\frac{d\alpha}{d\alpha} + \frac{\partial J}{\partial I_H}\frac{dI_H}{d\alpha} \tag{35}$$

The derivative of the weak form of the fluid problem (F from eq. (11)) is

$$\frac{dF}{d\alpha} = 0 \implies \frac{\partial F}{\partial(p, \boldsymbol{v})}\frac{d(p, \boldsymbol{v})}{d\alpha} + \frac{\partial F}{\partial \alpha}\frac{d\alpha}{d\alpha} = 0 \tag{36}$$

Therefore,

$$\frac{d(p,\boldsymbol{v})}{d\alpha} = -\left(\frac{\partial F}{\partial(p,\boldsymbol{v})}\right)^{-1}\frac{\partial F}{\partial\alpha} \tag{37}$$

The derivative of the weak form of the hemolysis model (from eq. (26), called F_H) is

$$\frac{dF_H}{d\alpha} = 0 \implies \frac{\partial F_H}{\partial(p,\boldsymbol{v})}\frac{d(p,\boldsymbol{v})}{d\alpha} + \frac{\partial F_H}{\partial\alpha}\frac{d\alpha}{d\alpha} + \frac{\partial F_H}{\partial I_H}\frac{dI_H}{d\alpha} = 0 \tag{38}$$

Therefore,

$$\frac{dI_H}{d\alpha} = -\left(\frac{\partial F_H}{\partial I_H}\right)^{-1}\left(\frac{\partial F_H}{\partial\alpha} + \frac{\partial F_H}{\partial(p,\boldsymbol{v})}\frac{d(p,\boldsymbol{v})}{d\alpha}\right) \tag{39}$$

Substituting eq. (37) in (39), and eqs. (37) and (39) in eq. (35),

$$\begin{aligned}\frac{dJ}{d\alpha} = \frac{\partial J}{\partial\alpha} &- \frac{\partial J}{\partial(p,\boldsymbol{v})}\left(\frac{\partial F}{\partial(p,\boldsymbol{v})}\right)^{-1}\frac{\partial F}{\partial\alpha} \\ &- \frac{\partial J}{\partial I_H}\left(\frac{\partial F_H}{\partial I_H}\right)^{-1}\left(\frac{\partial F_H}{\partial\alpha} - \frac{\partial F_H}{\partial(p,\boldsymbol{v})}\left(\frac{\partial F}{\partial(p,\boldsymbol{v})}\right)^{-1}\frac{\partial F}{\partial\alpha}\right)\end{aligned} \tag{40}$$

By taking the conjugate transpose of eq. (40),

$$\begin{aligned}\frac{dJ}{d\alpha}^* = \frac{\partial J}{\partial\alpha}^* &- \frac{\partial F}{\partial\alpha}^*\left[\left(\frac{\partial F}{\partial(p,\boldsymbol{v})}\right)^{-1}\right]^*\frac{\partial J}{\partial(p,\boldsymbol{v})}^* \\ &- \left(\frac{\partial F_H}{\partial\alpha}^* - \frac{\partial F}{\partial\alpha}^*\left[\left(\frac{\partial F}{\partial(p,\boldsymbol{v})}\right)^{-1}\right]^*\frac{\partial F_H}{\partial(p,\boldsymbol{v})}^*\right) \\ &\qquad\left[\left(\frac{\partial F_H}{\partial I_H}\right)^{-1}\right]^*\frac{\partial J}{\partial I_H}^*\end{aligned} \tag{41}$$

where " * " represents the conjugate transpose.

From eq. (41), the adjoint variables may be defined as:

$$\boldsymbol{\lambda}_J = \left[\left(\frac{\partial F}{\partial(p,\boldsymbol{v})}\right)^{-1}\right]^*\frac{\partial J}{\partial(p,\boldsymbol{v})}^* \tag{42}$$

$$\boldsymbol{\lambda}_H = \left[\left(\frac{\partial F}{\partial(p,\boldsymbol{v})}\right)^{-1}\right]^*\frac{\partial F_H}{\partial(p,\boldsymbol{v})}^* \tag{43}$$

$$\lambda_{JH} = \left[\left(\frac{\partial F_H}{\partial I_H}\right)^{-1}\right]^*\frac{\partial J}{\partial I_H}^* \tag{44}$$

From eqs. (42), (43) and (44), the adjoint equations become:

$$\left(\frac{\partial F}{\partial(p,\boldsymbol{v})}\right)^*\boldsymbol{\lambda}_J = \frac{\partial J}{\partial(p,\boldsymbol{v})}^* \tag{45}$$

$$\left(\frac{\partial F}{\partial(p,\boldsymbol{v})}\right)^*\boldsymbol{\lambda}_H = \frac{\partial F_H}{\partial(p,\boldsymbol{v})}^* \tag{46}$$

$$\left(\frac{\partial F_H}{\partial I_H}\right)^*\lambda_{JH} = \frac{\partial J}{\partial I_H}^* \tag{47}$$

With eqs. (42), (43) and (44), the sensitivity from eq. (41) becomes

$$\frac{dJ}{d\alpha}^* = \frac{\partial J}{\partial\alpha}^* - \frac{\partial F}{\partial\alpha}^*\boldsymbol{\lambda}_J - \left(\frac{\partial F_H}{\partial\alpha}^* - \frac{\partial F}{\partial\alpha}^*\boldsymbol{\lambda}_H\right)\lambda_{JH} \tag{48}$$

It can be highlighted that the derivative terms of eqs. (45), (46), (47), and (48) can be computed through automatic differentiation (AD).

5.6 Helmholtz pseudo-density filter

Some of the topology optimization results in this work use a Helmholtz filter for regularization. The Helmholtz filter is a PDE-based topology optimization pseudo-density filter, which has been proposed by Lazarov and Sigmund (2010). A schematic representation is shown in Fig. 5, where α is the original distribution of the design variable and α_f is the filtered distribution of the design variable.

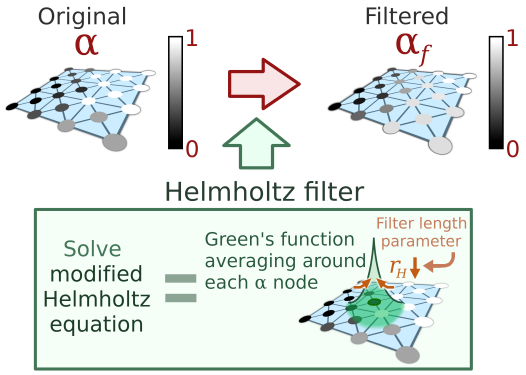

Fig. 5: Schematic representation of the application of a Helmholtz filter.

In Fig. 5, the application of a Helmholtz filter consists of weighting each value of the original design variable (α) with a Green's function, which is always positive and whose integral is equal to 1 (Lazarov and Sigmund, 2010). This function approaches a Dirac's delta function when using smaller filter length parameter values (r_H) ($\alpha_f \xrightarrow{r_H \to 0^+} \alpha$). This averaging is equivalent to solving a modified Helmholtz equation with homogeneous Neumann boundary conditions. The boundary value problem is then given by (Lazarov and Sigmund, 2010; Zauderer, 1989)

$$\begin{aligned} -r_H^2 \nabla^2 \alpha_f + \alpha_f = \alpha \quad & \text{in } \Omega \\ \frac{\partial \alpha_f}{\partial \boldsymbol{n}} = \mathbf{0} \quad & \text{on } \Gamma \end{aligned} \tag{49}$$

where α is the original design variable, α_f is the filtered design variable, and r_H is the filter length parameter.

By multiplying eq. (49) by a test function w_{HF} and integrating in the whole design domain, the weak form is given by

$$r_H^2 \int_\Omega (\nabla \alpha_f) \bullet \nabla w_{HF} r d\Omega + \int_\Omega \alpha_f w_{HF} r d\Omega - \int_\Omega \alpha w_{HF} r d\Omega = 0 \tag{50}$$

When using a Helmholtz filter, the value given by α_f is used instead of α in all other equations, and the sensitivities have to include the dependency of α_f with respect to α (from the chain rule ($\frac{dJ}{d\alpha} = \frac{dJ}{d\alpha_f}\frac{d\alpha_f}{d\alpha}$)) (Lazarov and Sigmund, 2010).

6 Numerical implementation of the optimization problem

The implementation of the finite element method is performed in the FEniCS platform (Logg et al., 2012), which relies on automatic differentiation and a high-level representation language for the weak form and functionals for later assembling the finite element matrices. The topology optimization method is implemented from the dolfin-adjoint library (Farrell et al., 2013; Mitusch et al., 2019), which automatically computes the adjoint model, and IPOPT (Interior-Point Optimization algorithm) (Wächter and Biegler, 2006), which is used as the optimization algorithm. IPOPT is based on a logarithmic barrier term that searches only in the feasible space (i.e., not allowing constraint violation), and relies on an augmentation that uses a line-search filter method, avoiding having to determine the exact value of the penalty parameter of the logarithmic barrier), and the dolfin-adjoint library has an interface for using it. Since the weak form of the fluid flow problem (eq. (11)) is nonlinear, the finite element method is solved through the Newton-Raphson method, by solving the corresponding linearized problems with MUMPS (MUltifrontal Massively Parallel sparse direct Solver) (Amestoy et al., 2001). On the other hand, the weak form of the hemolysis model (eq. (26)) is linear, which means that it may be directly solved by a linear solver, selected as an LU solver.

The topology optimization method is implemented as shown in Fig. 6. It starts with an initial guess of the topology. Then, the fluid flow problem is solved with FEniCS, followed by solving the hemolysis model equations also with FEniCS. These initial executions of the finite element method are used by dolfin-adjoint to automatically derive the adjoint model and, therefore, the sensitivity (as shown in eq. (48)). Then, the IPOPT optimization loop is started. The optimization loop continues until reaching the specified tolerance (convergence criterion).

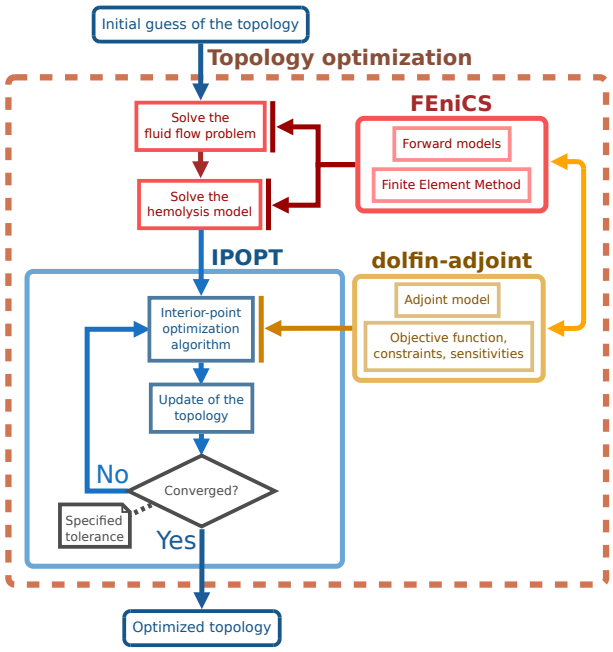

Fig. 6: Flowchart showing the numerical implementation of the topology optimization problem.

7 Numerical results

In the numerical results, the fluid is considered as blood, with the non-Newtonian dynamic viscosity ($\mu(\dot{\gamma}_\mathrm{m})$) from eqs. (6) and (30). Blood is assumed as incompressible, with a density (ρ) of 1056 kg/m^3 (Hinghofer-Szalkay and Greenleaf, 1987).

Structured finite element meshes are used, which are composed of rectangular partitions of 4 triangular elements each (see Fig. 7).

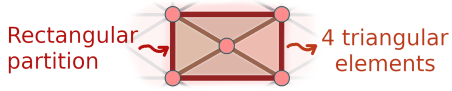

Fig. 7: Triangular elements distributed inside a rectangular partition.

For better numerical conditioning (when computing the weak form, the functionals and the sensitivities), and also for improving the convergence rate, the MMGS (Millimeters-Grams-Seconds) unit system is used, which means that the length and mass units are multiplied by a 10^3 factor when solving the finite element equations.

The convergence criterion of the Newton-Raphson method is given from an absolute tolerance of 10^{-10}, and a relative tolerance of 10^{-9}. The convergence criterion for the optimization relies on a desired tolerance of 10^{-10} for the optimality error of the IPOPT barrier problem, which is essentially given from to the maximum norm of each KKT condition (Wächter and Biegler, 2006).

No external body forces are considered for the numerical examples ($\rho \boldsymbol{f} = (0,\ 0,\ 0)$), and the specified fluid volume fraction (f) is chosen as 30%. The porous medium is assumed to be rotating the same as the reference frame, which means that $\boldsymbol{v}_{\text{mat}} = \boldsymbol{v}$. Also, $\kappa_{\min} = 0$ kg/(m^3 s). The initial guess for the pseudo-density (design variable) distribution is a uniform distribution of $\alpha = f - 1\%$, where f is the specified fluid volume fraction and 1% is a margin for the initial guess not to violate the volume constraint (because of the numerical accuracy of the calculations). The plots of the optimized topologies consider the values of the pseudo-density (design variable) in the center of each finite element. The letter n is used to denote rotation in rpm, and the greek letter ω is used to denote rotation in rad/s.

The pseudo-density (design variable) values of the optimized topologies are post-processed by a threshold function (eq. (51)), and the resulting contour is smoothened in order to reduce "jagged mesh" effects in the final simulations of the optimized topologies.

$$\alpha_{\text{th}} = \begin{cases} 1 \text{ (fluid), if } \alpha \geqslant 0.5 \\ 0 \text{ (solid), if } \alpha < 0.5 \end{cases} \tag{51}$$

As well as any post-processing scheme, some inherent small deviation is possibly induced in the post-processed mesh with respect to the optimized topology given from the distribution of the design variable (α).

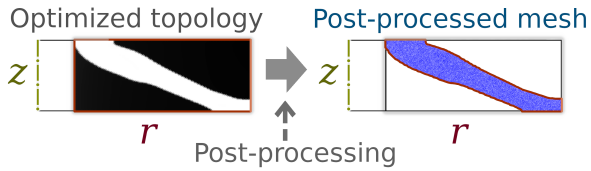

Fig. 8: Post-processing used for the optimized topologies.

For simplicity, the Reynolds number is given as the maximum value of the local Reynolds number based on the external diameter:

$$\text{Re}_{\text{ext},\,\ell} = \frac{\mu(\dot{\gamma_{\text{m}}})\,|\boldsymbol{v}_{\text{abs}}|\,(2r_{ext})}{\rho} \tag{52}$$

where the non-Newtonian viscosity ($\mu(\dot{\gamma_{\text{m}}})$) may vary in each position of the computational domain, the absolute velocity ($\boldsymbol{v}_{\text{abs}}$) varies in each position of the computational domain, r_{ext} is the external radius of the computational domain, and ρ is the density.

The variation of (static) pressure is computed for the Tesla blood pump rotor, because it is normally evaluated for blood pumps. The total ("stagnation") pressure is also computed for the Tesla blood pump rotor, because the volute (which converts dynamic pressure into static pressure) is not being considered in this work. The variations of (static) pressure (Δp) and total ("stagnation") pressure (Δp_T) are given by

$$\Delta p = \overline{p}_{out} - \overline{p}_{in} = \frac{\int_{\Gamma_{\text{out}}} p 2\pi r d\Gamma_{\text{out}}}{\int_{\Gamma_{\text{out}}} 2\pi r d\Gamma_{\text{out}}} - \frac{\int_{\Gamma_{\text{in}}} p 2\pi r d\Gamma_{\text{in}}}{\int_{\Gamma_{\text{in}}} 2\pi r d\Gamma_{\text{in}}} \tag{53}$$

$$\Delta p_T = \overline{p}_{T,out} - \overline{p}_{T,in} = \frac{\int_{\Gamma_{\text{out}}} \left(p + \frac{\rho|\boldsymbol{v}_{\text{abs}}|^2}{2}\right) 2\pi r d\Gamma_{\text{out}}}{\int_{\Gamma_{\text{out}}} 2\pi r d\Gamma_{\text{out}}} - \frac{\int_{\Gamma_{\text{in}}} \left(p + \frac{\rho|\boldsymbol{v}_{\text{abs}}|^2}{2}\right) 2\pi r d\Gamma_{\text{in}}}{\int_{\Gamma_{\text{in}}} 2\pi r d\Gamma_{\text{in}}} \tag{54}$$

The pressure head is computed as shown in eq. (55). When it is higher than zero, it may be used to characterize the capacity of the fluid flow device to pump fluid.

$$H = \frac{1}{Q}\left[\int_{\Gamma_{\text{in}}} \left(\frac{p}{\rho g} + \frac{|\boldsymbol{v}_{\text{abs}}|^2}{2g}\right) \boldsymbol{v}\bullet\boldsymbol{n} 2\pi r d\Gamma_{\text{in}} + \int_{\Gamma_{\text{out}}} \left(\frac{p}{\rho g} + \frac{|\boldsymbol{v}_{\text{abs}}|^2}{2g}\right) \boldsymbol{v}\bullet\boldsymbol{n} 2\pi r d\Gamma_{\text{out}}\right] \tag{55}$$

where g is the gravity acceleration (9.8 m/s^2).

The isentropic efficiency may be used to characterize the efficiency of the fluid flow device Rey Ladino (2004); Sonntag and Borgnakke (2013), and may be given as

$$\eta_s = \frac{P_{ideal}}{P_{real}} = \frac{\Delta h_s}{P_f/\dot{m}} = \frac{gH}{P_f/\dot{m}} \tag{56}$$

where $\dot{m} = \rho Q$ is the mass flow rate, and $\Delta h_s = gH$ is the variation of specific enthalpy (specific work) in the ideal process (Sonntag and Borgnakke, 2013). P_f is the fluid power given by

$$P_f = \oint_\Gamma \boldsymbol{\omega} \bullet (\boldsymbol{s} \wedge \boldsymbol{v}_{\text{abs}}) \rho \boldsymbol{v}_{\text{abs}} \bullet \boldsymbol{n} 2\pi r d\Gamma \tag{57}$$

7.1 Design domain and mesh

The numerical example consists of the design of a Tesla blood pump with a vertical inlet and a center shaft (Alonso et al., 2019). The design domain is shown in Fig. 9.

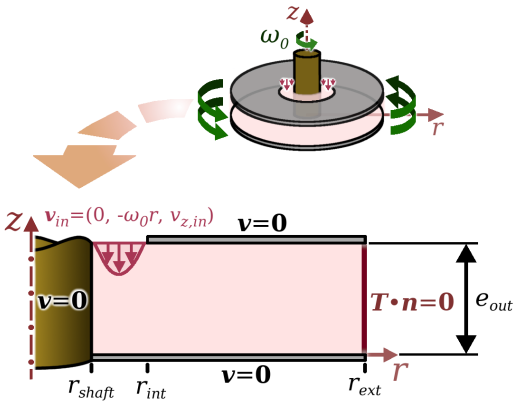

Fig. 9: Design domain for the Tesla blood pump design.

The dimensions from Fig. 9 are $r_{shaft} = 2.6$ mm, $r_{int} = 5$ mm, $e_{out} = 5$ mm, and $r_{ext} = 15$ mm. The inlet velocity profile is parabolic. The mesh is composed of 100 radial and 46 axial rectangular partitions of crossed triangular elements, totaling 10,277 nodes and 20,240 elements (see Fig. 10).

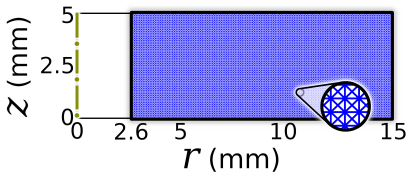

Fig. 10: Mesh used in the Tesla blood pump design.

A straight-channel Tesla-type pump (see Fig. 11) is simulated in order to compute the reference values for comparing with the optimized results in the following Sections.

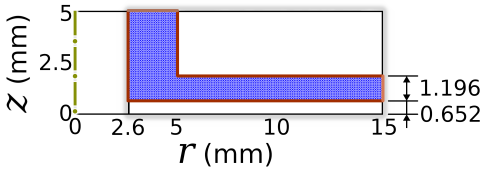

Fig. 11: Reference straight-channel Tesla-type pump for comparing with the optimized results.

7.2 Topology optimization results

The effect of the hemolysis index in the multi-objective function (eq. (33)) is analyzed for $w_H = 0.1$, 0.5 and 0.9. The case for $w_H = 1.0$ is not evaluated, because the topology optimization is unable to form a fluid flow path in the optimized topology, with the outlet completely blocked. This "completely blocked" outlet makes sense, because, if there is no fluid flow, the hemolysis index becomes minimal. The flow rates being considered are 0.5 L/min, 1 L/min and 2 L/min, and the rotations are 0 rpm, 1500 rpm and 3000 rpm. The optimized results for the two objective functions (total hemolysis index and relative energy dissipation) are shown in Fig. 12. Since the values of relative energy dissipation at 0 rpm are positive (due to the inertial term of eq. (32) being zero at 0 rpm), in order to plot all relative energy dissipation values in the same figure, the Matplotlib (Hunter, 2007) "symlog" scheme is used, in which a logarithmic scale is used as "$\text{sgn}(\Phi_{\text{rel}}) \log_{10} |\Phi_{\text{rel}}|$" ("$\text{sgn}(\Phi_{\text{rel}})$" is the signal of Φ_{rel}), except near the zero value, around which a linear scale is used. Among the optimized results for 0 rpm, 1500 rpm and 3000 rpm, the only results in which the fluid flow device does not operate as a pump, correspond to 0 rpm, because there is only viscous dissipation inside the fluid flow device, without the fluid receiving rotational energy. This fact can also be noticed when computing the pressure head values, since the pressure head needs to be positive for the fluid flow device to pump fluid (i.e., to act as a pump).

The optimization parameters that have been used in this work are shown in Table 1.

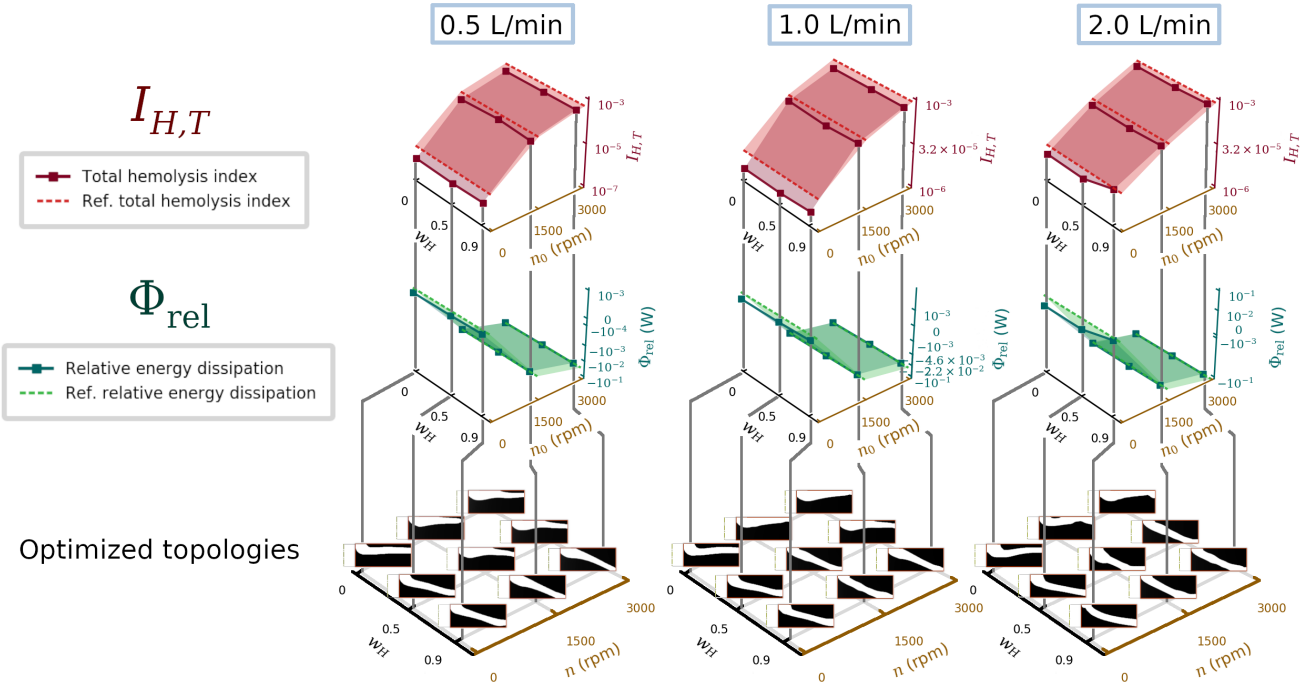

Fig. 12: Total hemolysis index and relative energy dissipation for the topology optimization considering the effect of the flow rate and rotation.

Table 1: Optimization parameters for each optimized topology* ($q = 1$).

Flow rate (Q) (L/min)	Rotation (n_0) (rpm)	$\kappa_{\max}$ ($\times 10^8 \mu_\infty$) (kg/(m^{3}s))
0.5	0	5
	1500	50
	3000	100
1.0	0	5
	1500	50
	3000	80
2.0	0	5
	1500	80
	3000	100

* With the exception of the optimized results for "0.5 L/min, 0 rpm", "0.5 L/min, 1500 rpm, $w_H = 0$" and "0.5 L/min, 1500 rpm, $w_H = 0.5$", all other results consider a Helmholtz pseudo-density filter (Section 5.6) for better stabilizing the discrete optimized topologies. The filter length parameter (r_H) is chosen as the value $r_H = 0.0564$ mm.

The convergence curve for the optimized topology for $w_H = 0.5$, 1 L/min and 1500 rpm is shown in Fig. 13. In the otimized results, the maximum Reynolds number is achieved at 3000 rpm, where, for all flow rates, $\mathrm{Re}_{\mathrm{ext},\,\ell} \approx 4.3 \times 10^4$. Since the transition Reynolds number in conventional pumps is in the order of 10^6 Sabersky et al. (1971); Wu (2007), 4.3×10^4 should correspond to laminar flow.

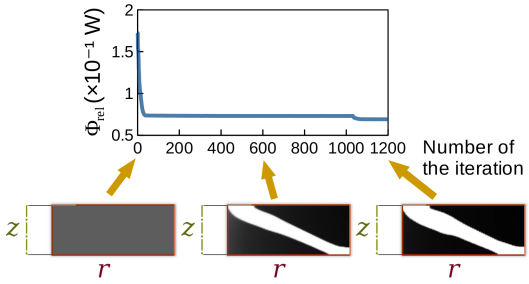

Fig. 13: Convergence curve for the optimized topology for $w_H = 0.5$, 1 L/min and 1500 rpm.

In Fig. 12, the reference values are shown by dashed lines, while the full lines correspond to the optimized topologies. As expected, higher rotations lead to higher total hemolysis index ($I_{H,T}$) values (i.e., higher hemolysis), and smaller relative energy dissipation values (Φ_{rel}), due to the rotational pumping motion (i.e., the inertial term in the relative energy dissipation (eq. (32))), which also leads to negative relative energy dissipation values (i.e., the fluid receiving more energy than dissipating it). As can be noticed from the total

hemolysis index ($I_{H,T}$) plots, the optimized topologies lead to smaller hemolysis than the reference values. This can be explained by the fact that the optimized topologies feature a "rounded" curve near the inlet, meaning that the fluid flow has a smoother change of direction in the optimized topologies than in the reference (Fig. 11), and which should lead to less induced stress over the RBCs. Also, the optimized topologies featuring inclined channels have smaller changes of fluid flow direction, which should also contribute to reducing the total hemolysis index. From the relative energy dissipation values (Φ_{rel}), it can be noticed that, at 0 rpm the optimized topologies lead to smaller relative energy dissipation values, but that difference is diminished at higher rotations. This difference may be better visualized in Fig. 14a, which shows the influence of the rotation in the topology optimization for 1 L/min and $w_H = 0.5$, in which the relative energy dissipation of the optimized topology achieves a higher value than the reference. Fig. 14a shows an improvement of about 50% of the total hemolysis index of the optimized topology with respect to the reference values. Fig. 14b shows the pressure head and isentropic efficiency, but no significant difference can be noticed comparing the optimized and reference values. For the variation of total/static pressure (Fig. 14c), the difference is also small.

The optimized topologies from Fig. 14 show that the effect of the relative energy dissipation in the optimized topology seems to increase at higher rotations, given that the optimized topology connects to an outlet located at a higher height when the rotation is increased. This effect can also be seen in Fig. 12, where the optimized channel for $w_H = 0.5$ features an outlet located at a higher height, but, for $w_H = 0.9$, due to the higher effect of the total hemolysis index, the optimized topologies feature inclined channels (i.e., inclined disks). The higher position of the channels at lower w_H values (with the exception of 0 rpm) is probably due to the rotational motion of the fluid flow, which creates an inertial effect that creates a tendency for continuing the fluid motion at the same height. These "inclined disk"-like topologies slightly ressemble some commercial Tesla pump devices that feature conical-shaped disks (BPX-80 BIO-Pump Plus (Medtronic®), CentriFlux BR-100 (Braile® Biomédica)).

The effect of the flow rate from Fig. 12 is separated in Fig. 15, for 1500 rpm and $w_H = 0.5$. As can be noticed in Fig. 15a, the total hemolysis index of the optimized topologies is much lower than the reference, and the relative energy dissipation is slightly smaller than the reference. One effect that can be noticed is that the total hemolysis index increases from 0.5 L/min to 1 L/min, but decreases from 1 L/min to 2 L/min. This is probably due, in the reference, to the fluid flowing close to the upper and lower surfaces for 0.5 L/min and 1 L/min, but closer to the lower surface for 2 L/min, which means that the shear stress is more concentrated below and with a higher velocity. In the case of the optimized topology, this change may be due to the change in topology, where the shear stress effect may be reduced on the straighter channel near the outlet. As can be noticed, the pressure head and isentropic efficiencies for the reference at 2 L/min in Fig. 15b is extremely low (around 0.003 m and 1%). This is because the minimum rotation required for the fluid flow device to act as a pump (i.e., with positive value for the pressure head) is higher for higher flow rates. It can be noticed that the pressure head and isentropic efficiency are higher for lower flow rates, which is a hint to this behavior. In the case of the reference at 2 L/min, the transition of behavior from a "dissipation channel" to a "pump-type device" is near 1500 rpm, which explains the extremely low pressure head and isentropic efficiency values at 2 L/min. This effect is more softened for the optimized topology for 2 L/min, because the new format changed the rotation of this transition of behavior to a lower value. Fig. 15c shows that the variation of total/static pressure is better for the optimized topologies for most cases, which should be due to the smoother change in curvature in the optimized results.

With respect to the composition of the multi-objective function, this effect is separated from Fig. 12 in Fig. 16, for 0.5 L/min and 1500 rpm. In this configuration, from Fig. 16, the values for the optimized topologies show a Pareto-like effect, in which the relative energy dissipation is worsened for higher w_H values, while the total hemolysis index improves (except from $w_H = 0.9$, where the total hemolysis index slightly worsens) due to the inclined channel/disks. In comparison to the reference values, the total hemolysis indices of the optimized topologies is always better, most probably due to the sharp change in flow direction present in the reference, which, due to these higher velocity gradients, should lead to higher hemolysis. However, the relative energy dissipation values gets worse than the reference for $w_H = 0.9$ probably due to "overprioritizing" the minimization of hemolysis in relation to the relative energy dissipation. This "overprioritization" led to a more "constantly thicker" channel at $w_H = 0.9$, in comparison to the thinner channel at $w_H = 0.5$, which portrays a slight reduction in sectional area from the inlet to the outlet. In Fig. 16a, the inclined channels/disks in the optimized topologies ended up improving the pressure head value, but the isentropic efficiency slightly drops

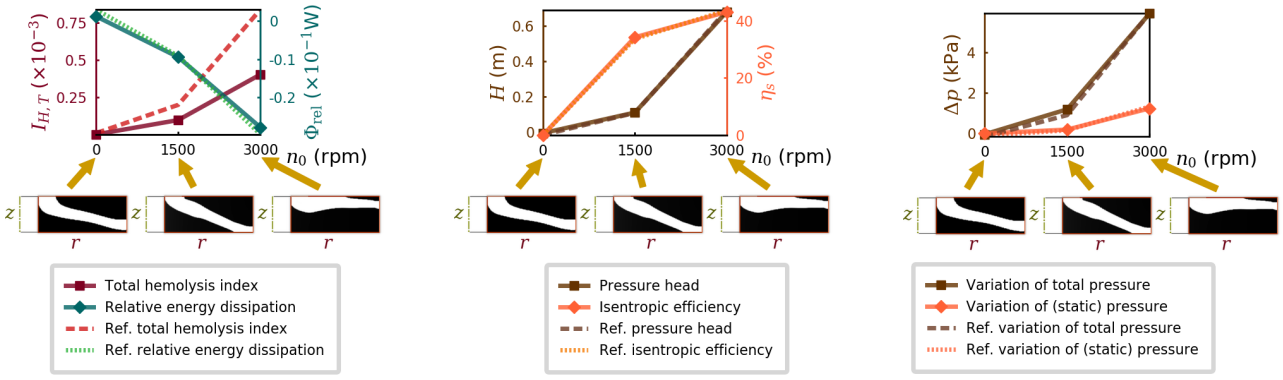

(a) Total hemolysis index and relative energy dissipation.

(b) Pressure head and isentropic efficiency.

(c) Variation of total and static pressures.

Fig. 14: Topology optimization results for different rotations (n_0) (for 1 L/min and $w_H = 0.5$).

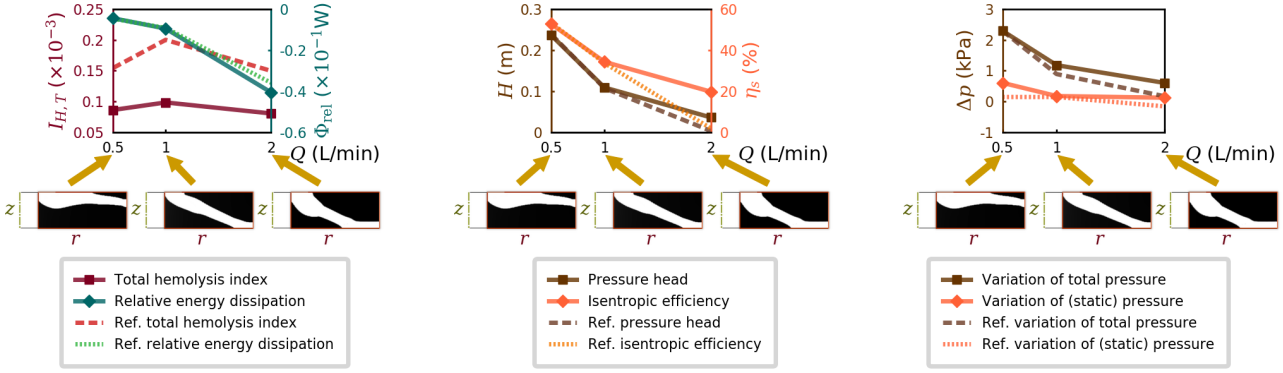

(a) Total hemolysis index and relative energy dissipation.

(b) Pressure head and isentropic efficiency.

(c) Variation of total and static pressures.

Fig. 15: Topology optimization results for different flow rates (Q) (for 1500 rpm and $w_H = 0.5$).

at $w_H = 0.9$, which may also be caused by the same effect observed in the total hemolysis index from $w_H = 0.5$ to $w_H = 0.9$. With respect to the variation of total/static pressure (Fig. 16c), the optimized results are better than the reference, leading to higher variation of pressure values.

7.3 Simulation of the optimized result for $w_H = 0.5$, 1 L/min and 1500 rpm

The optimized topology for $w_H = 0.5$, 1 L/min and 1500 rpm, is simulated and is shown in Fig. 17. In Fig. 17, the 3D representation shows how the optimized topology is interpreted, with two specially shaped rotating disks. The pressure (p) plot shows that the main pressure increase occurs in the middle of the channel, which may mean that, if this length is increased (for larger Tesla-type pump devices), the pressure should also increase more. From the plot of the radial-axial velocity ((v_r, v_z)), two low velocity zones can be noticed. Both zones do not consist of flow recirculation, corresponding to: (zone at higher height) A low-velocity flow redirection; (zone at lower height) Low velocity due to the presence of two separated boundary layers. The plot of the relative tangential velocity (v_θ) shows, as expected, that the higher tangential velocity is located on the rotating wall surfaces ($v_\theta = 0$, $v_{\theta,\text{abs}} = \omega_0 r$) and its value is lower where it is farther from the wall, due to the "dragging" effect from the Tesla principle.

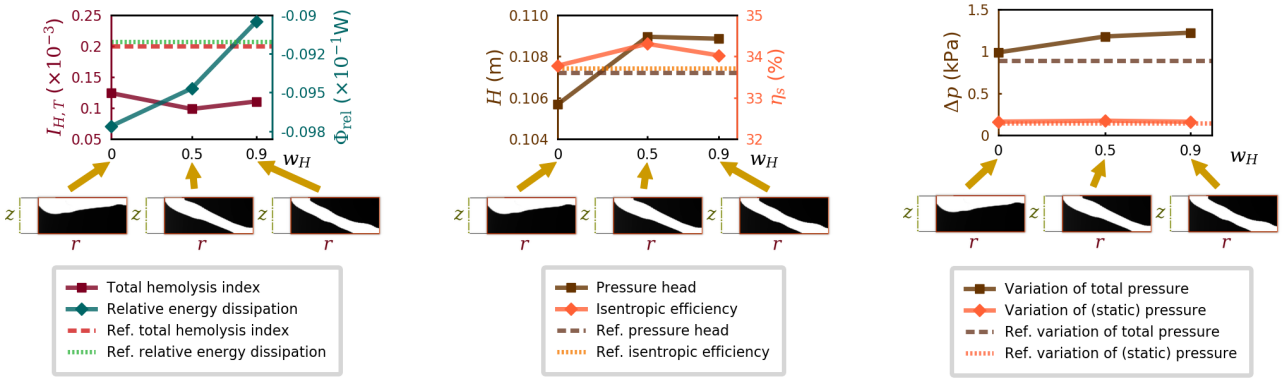

(a) Total hemolysis index and relative energy dissipation.

(b) Pressure head and isentropic efficiency.

(c) Variation of total and static pressures.

Fig. 16: Topology optimization results for different w_H values (for 1 L/min and 1500 rpm).

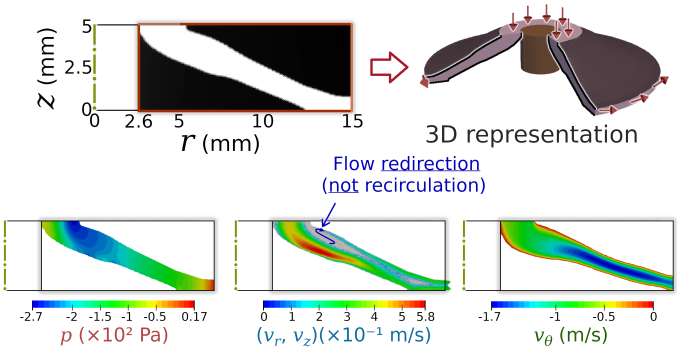

Fig. 17: Optimized topology, 3D representation, pressure and velocity for $w_H = 0.5$, 1 L/min and 1500 rpm.

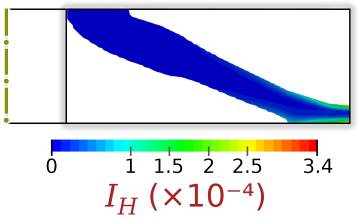

(a) Total hemolysis index (normal scale).

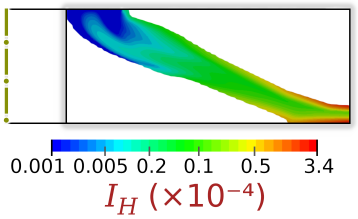

(b) Total hemolysis index (logarithmic scale).

Fig. 18: Total hemolysis index for the optimized topology for $w_H = 0.5$, 1 L/min and 1500 rpm.

The local hemolysis index (I_H) is plotted in Fig. 18. As can be seen in Fig. 18a, the local hemolysis index is higher near the walls closer to the outlet, probably due to the higher shear stresses resulting from the higher fluid flow velocity and rotation. In order to better visualize the local hemolysis index distribution, Fig. 18b shows the same plot in logarithmic scale. As can be seen, the generation of hemolysis is small and approximately uniform in the "channel region" in the middle of the optimized topology, and highly increases near walls at higher radii due to the effect observed in Fig. 18a.

Since the fluid model for blood used in this work is non-Newtonian, the plot of the non-Newtonian viscosity values is shown in Fig. 19. As can be seen, the non-Newtonian viscosity is slightly higher at the inlet and keeps being higher near the middle of the channel section of the optimized topology. This higher viscosity means that the low-velocity recirculation regions shown in Fig. 17 feature slightly higher viscosity values. Near walls, the non-Newtonian viscosity is smaller due to the higher shear stress.

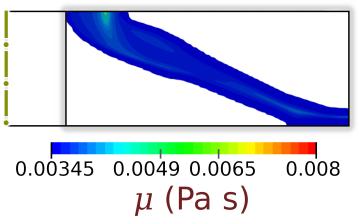

Fig. 19: Non-Newtonian viscosity the optimized topology for $w_H = 0.5$, 1 L/min and 1500 rpm.

8 Conclusions

In this work, the topology optimization method is formulated to take into account a hemolysis model given by a differential equation ("asymptotically consistent damage index"), which has not been performed in previous works. In order to consider the sensitivity of the hemolysis index, the sensitivities of the weak forms of the fluid flow problem and hemolysis models are combined, which, in this work, is automated by using the dolfin-adjoint library. This approach is illustrated by a 2D swirl flow (Tesla-type) blood pump device considering a non-Newtonian fluid (blood).

The numerical results considers the application of topology optimization for two objective functions (relative energy dissipation and total hemolysis index), showing that the total hemolysis index objective function leads to different optimized topologies. In the case of Tesla-type blood pump devices, it creates a tendency for "inclined disk"-like topologies, while the relative energy dissipation function creates a tendency for "straighter disk"-like topologies. The "inclined disk"-like topologies slightly resemble some commercial Tesla pump devices that feature conical-shaped disks.

As future work, it is suggested to consider other hemolysis models, other blood damage sources (such as thrombosis), thermal effects and turbulence.

9 Replication of results

The implementation in the FEniCS platform is direct from the description provided of the equations and numerical implementation in this article, because FEniCS is based on a high-level description for the variational formulation (UFL), automating the generation of the matrix equations.

It may be reminded that, in the case of 2D swirl flow, the coordinates are cylindrical (i.e., the differential operators ("`grad`", "`curl`", "`div`") must be programmed by hand by using the "`Dx(var,component_num)`" or "`var.dx(component_num)`" functions, because the default operators provided by FEniCS assume Cartesian coordinates). The pseudocode of the implementation is indicated in Algorithm 1, where the main FEniCS/dolfin-adjoint functions that are being used are represented between parentheses. When using dolfin-adjoint, the dolfin-adjoint library provides an interface to IPOPT.

Funding information This research was partly supported by CNPq (Brazilian Research Council) and FAPESP (São Paulo Research Foundation). The authors thank the supporting institutions. The first author thanks the financial support of FAPESP under grant 2017/27049-0. The second author thanks the financial support of CNPq (National Council for Research and Development) under grant 302658/2018-1 and of FAPESP under grant 2013/24434-0. The authors also acknowledge the support of the RCGI (Research Centre for Gas Innovation), hosted by the University of São Paulo (USP) and sponsored by FAPESP (2014/50279-4) and Shell Brazil.

Compliance with ethical standards

Conflict of interest The authors declare that they have no conflict of interest.

Algorithm 1 Pseudocode of the implementation

Input parameters: Flow rate, rotation, dimensions, optimization parameters and constants
Result: Optimized topology (optimized distribution of the design variable) and its post-processed simulation
1 Generate the finite element mesh ("`RectangleMesh`")
2 Prepare the state variables (pressure and velocity) and design variable (pseudo-density) (see Section 3.2) (CG2 "`VectorElement`" with "`dim=3`" (velocity), CG1 "`FiniteElement`" (pressure and pseudo-density), "`MixedElement`" (for pressure and velocity), "`FunctionSpace`")
3 Define the Dirichlet boundary conditions (see eq. (8)) ("`DirichletBC`")
4 Define the bounds of the design variable ([0, 1]) (see eq. (31))
5 Define the initial guess of the topology (i.e., the initial values of the design variable) ("`interpolate`")
6 For each desired optimization scheme (i.e., step):
  6.1 Clean up dolfin-adjoint annotations, in order to start a new automatic derivation of the adjoint model (i.e., define a new "tape" for dolfin-adjoint) ("`set_working_tape(Tape())`")
  6.2 Prepare the finite element method
    6.2.1 Define the material model for the inverse permeability (eq. (29))
    6.2.2 Define the non-Newtonian viscosity (eq. (6) or eq. (30))
    6.2.3 Define the weak form of the non-Newtonian flow problem (eq. (11))
    6.2.4 Define the non-linear solver (Newton-Raphson method) for the fluid flow simulation ("`NonlinearVariationalProblem`", "`NonlinearVariationalSolver`", set parameter `,linear_solver,` to `,mumps,`)
    6.2.5 Solve the fluid flow equations. When performing this operation, dolfin-adjoint automatically annotates the corresponding adjoint model
    6.2.5 Define the weak form of the hemolysis model (eq. (26))
    6.2.6 Define the linear solver (LU solver) for the hemolysis model ("`LinearVariationalProblem`", "`LinearVariationalSolver`")
    6.2.5 Solve the hemolysis model. When performing this operation, dolfin-adjoint automatically annotates the corresponding adjoint model
  6.3 Finish preparing the topology optimization problem
    6.3.1 Set the pseudo-density as the design variable ("`Control`")
    6.3.2 Define the objective function (eq. (33)) ("`assemble`")
    6.3.3 Define the volume constraint (see eq. (31)) ("`UFLInequalityConstraint`")
    6.3.4 Prepare the IPOPT solver for topology optimization ("`ReducedFunctional`", "`MinimizationProblem`", "`IPOPTSolver`")
  6.4 Run the IPOPT solver (see Fig. 6) ("`[IPOPTSolver].solve`")
7 Post-process the optimized topology
8 Set up and solve the finite element method for the post-processed mesh

References

Abraham F, Behr M, Heinkenschloss M (2005) Shape optimization in steady blood flow: a numerical study of non-newtonian effects. Computer methods in biomechanics and biomedical engineering 8(2):127–137

Alemu Y, Bluestein D (2007) Flow-induced platelet activation and damage accumulation in a mechanical heart valve: numerical studies. Artificial organs 31(9):677–688

Alimohamadi H, Imani M, Shojaeizadeh M (2014) Numerical simulation of porosity effect on blood flow pattern and atherosclerotic plaques temperature. International journal of technology enhancements and emerging engineering research 2(10)

Alonso DH, de Sá LFN, Saenz JSR, Silva ECN (2018) Topology optimization applied to the design of 2d swirl flow devices. Structural and Multidisciplinary Optimization 58(6):2341–2364, DOI 10.1007/s00158-018-2078-0, URL `https://doi.org/10.1007/s00158-018-2078-0`

Alonso DH, de Sá LFN, Saenz JSR, Silva ECN (2019) Topology optimization based on a two-dimensional swirl flow model of tesla-type pump devices. Computers & Mathematics with Applications 77(9):2499 – 2533, DOI https://doi.org/10.1016/j.camwa.2018.12.035, URL `http://www.sciencedirect.com/science/article/pii/S0898122118307338`

Alonso DH, Saenz JSR, Silva ECN (2020) Non-newtonian laminar 2d swirl flow design by the topology optimization method. Structural and Multidisciplinary Optimization 62(1):299–321, DOI https://doi.org/10.1007/s00158-020-02499-2, URL `https://link.springer.com/article/10.1007%2Fs00158-020-02499-2`

Amestoy PR, Duff IS, Koster J, L'Excellent JY (2001) A fully asynchronous multifrontal solver using distributed dynamic scheduling. SIAM Journal on Matrix Analysis and Applications 23(1):15–41

Andreasen CS, Gersborg AR, Sigmund O (2009) Topology optimization of microfluidic mixers. International Journal for Numerical Methods in Fluids 61:498–513, URL `http://dx.doi.org/10.1002/fld.1964`

Antaki JF, Ghattas O, Burgreen GW, He B (1995) Computational flow optimization of rotary blood pump components. Artificial Organs 19(7):608–615

Apel J, Paul R, Klaus S, Siess T, Reul H (2001) Assessment of hemolysis related quantities in a microaxial blood pump by computational fluid dynamics. Artificial Organs 25(5):341–347, DOI 10.1046/j.1525-1594.2001.025005341.x,

URL https://onlinelibrary.wiley.com/doi/abs/10.1046/j.1525-1594.2001.025005341.x, https://onlinelibrary.wiley.com/doi/pdf/10.1046/j.1525-1594.2001.025005341.x

Arora D, Behr M, Pasquali M (2004) A tensor-based measure for estimating blood damage. Artificial Organs 28(11):1002–1015

Arora D, Behr M, Pasquali M (2006a) Errata. Artificial Organs 30(11):892–892, DOI 10.1111/j.1525-1594.2006.00318.x, URL https://onlinelibrary.wiley.com/doi/abs/10.1111/j.1525-1594.2006.00318.x, https://onlinelibrary.wiley.com/doi/pdf/10.1111/j.1525-1594.2006.00318.x

Arora D, Behr M, Pasquali M (2006b) Hemolysis estimation in a centrifugal blood pump using a tensor-based measure. Artificial organs 30(7):539–547

Arora D, Behr M, Pasquali M (2012) Errata. Artificial Organs 36(5):500–500, DOI 10.1111/j.1525-1594.2012.01491.x, URL https://onlinelibrary.wiley.com/doi/abs/10.1111/j.1525-1594.2012.01491.x, https://onlinelibrary.wiley.com/doi/pdf/10.1111/j.1525-1594.2012.01491.x

ASTM F1841-97 (1997) Standard practice for assessment of hemolysis in continuous flow blood pumps. Tech. rep., ASTM International, West Conshohocken, PA, URL http://www.astm.org/cgi-bin/resolver.cgi?F1841-97

Barthes-Biesel D, Rallison J (1981) The time-dependent deformation of a capsule freely suspended in a linear shear flow. Journal of Fluid Mechanics 113:251–267

Bear J (2018) Modeling Phenomena of Flow and Transport in Porous Media, vol 31. Springer

Behbahani M, Behr M, Hormes M, Steinseifer U, Arora D, CORONADO O, Pasquali M (2009) A review of computational fluid dynamics analysis of blood pumps 20:363 – 397

Billett HH (1990) Hemoglobin and hematocrit. In: Clinical Methods: The History, Physical, and Laboratory Examinations. 3rd edition, Butterworths

Bird RB, Armstrong RC, Hassager O (1987) Dynamics of polymeric liquids, Volume 1: Fluid mechanics, 1st edn. John Wiley & Sons

Bludszuweit C (1995) Three-dimensional numerical prediction of stress loading of blood particles in a centrifugal pump. Artificial Organs 19(7):590–596

Borrvall T, Petersson J (2003) Topology optimization of fluids in stokes flow. International Journal for Numerical Methods in Fluids 41(1):77–107, DOI 10.1002/fld.426, URL http://dx.doi.org/10.1002/fld.426

Brezzi F, Fortin M (1991) Mixed and Hybrid Finite Element Methods. Springer-Verlag, Berlin, Heidelberg

Brinkman HC (1947) A calculation of the viscous force exerted by a flowing fluid on a dense swarm of particles. Journal of applied sciences research A1:27–34

Cho YI, Kenssey KR (1991) Effects of the non-newtonian viscosity of blood on flows in a diseased arterial vessel. part 1: Steady flows. Biorheology 28:241–262

Cimolin F, Discacciati M (2013) Navier–stokes/forchheimer models for filtration through porous media. Applied Numerical Mathematics 72:205–224

Darcy HPG (1856) Les Fontaines publiques de la ville de Dijon. Exposition et application des principes à suivre et des formules à employer dans les questions de distribution d'eau, etc. V. Dalamont

De Wachter D, Verdonck P (2002) Numerical calculation of hemolysis levels in peripheral hemodialysis cannulas. Artificial organs 26(7):576–582

Deng Y, Liu Z, Wu Y (2013) Topology optimization of steady and unsteady incompressible navier—stokes flows driven by body forces. Struct Multidiscip Optim 47(4):555–570, DOI 10.1007/s00158-012-0847-8, URL http://dx.doi.org/10.1007/s00158-012-0847-8

Dilgen CB, Dilgen SB, Fuhrman DR, Sigmund O, Lazarov BS (2018) Topology optimization of turbulent flows. Computer Methods in Applied Mechanics and Engineering 331:363–393, DOI 10.1016/j.cma.2017.11.029

Dodsworth L (2016) Operational parametric study of a prototype tesla pump. Master's thesis, Dalhousie University

Dorman FD, Murphy TE, Blackshear PL (1966) An application of the tesla viscous flow turbine to pumping blood: Mechanical devices to assist the failing heart. national research council. In: National Academy of Science, pp 119–128

Duan X, Li F, Qin X (2016) Topology optimization of incompressible navier–stokes problem by level set based adaptive mesh method. Computers & Mathematics with Applications 72(4):1131 – 1141, DOI https://doi.org/10.1016/j.camwa.2016.06.034, URL http://www.sciencedirect.com/science/article/pii/S0898122116303662

Evgrafov A (2004) Topology optimization of navier-stokes equations. In: Nordic MPS 2004. The Ninth Meeting of the Nordic Section of the Mathematical Programming Society, Linköping University Electronic Press, 014, pp 37–55

Evgrafov A (2006) Topology optimization of slightly compressible fluids. ZAMM-Journal of Applied

Mathematics and Mechanics/Zeitschrift für Angewandte Mathematik und Mechanik 86(1):46–62

Farinas MI, Garon A, Lacasse D, N'dri D (2006) Asymptotically consistent numerical approximation of hemolysis. Journal of Biomechanical Engineering 128(5):688–696, DOI 10.1115/1.2241663, URL https://doi.org/10.1115/1.2241663, https://asmedigitalcollection.asme.org/biomechanical/article-pdf/128/5/688/5621900/688_1.pdf

Farrell PE, Ham DA, Funke SW, Rognes ME (2013) Automated derivation of the adjoint of high-level transient finite element programs. SIAM Journal on Scientific Computing 35(4):C369–C393

Forchheimer P (1901) Wasserbewegung durch boden. Z Ver Deutsch, Ing 45:1782–1788

Fraser K, Taskin M, Zhang T, Griffith B, Wu Z (2010) Comparison of shear stress, residence time and lagrangian estimates of hemolysis in different ventricular assist devices. In: 26th Southern Biomedical Engineering Conference SBEC 2010, April 30-May 2, 2010, College Park, Maryland, USA, Springer, pp 548–551

Fraser KH, Taskin ME, Griffith BP, Wu ZJ (2011) The use of computational fluid dynamics in the development of ventricular assist devices. Medical Engineering & Physics 33(3):263–280, DOI 10.1016/j.medengphy.2010.10.014, URL http://opus.bath.ac.uk/43258/

Garon A, Farinas MI (2004) Fast three-dimensional numerical hemolysis approximation. Artificial Organs 28(11):1016–1025

Geertsma J (1974) Estimating the coefficient of inertial resistance in fluid flow through porous media. Society of Petroleum Engineers Journal 14(05):445–450

Ghattas O, He B, Antaki JF, et al. (1995) Shape optimization of navier-stokes flows with application to optimal design of artificial heart components. Tech. rep., Carnegie Institute of Technology, Department of Civil and Environmental Engineering

Giersiepen M, Wurzinger L, Opitz R, Reul H (1990) Estimation of shear stress-related blood damage in heart valve prostheses-in vitro comparison of 25 aortic valves. The International journal of artificial organs 13(5):300–306

Gijsen FJH, van de Vosse FN, Janssen JD (1999) The influence of the non-newtonian properties of blood on the flow in large arteries: steady flow in a carotid bifurcation model. Journal of Biomechanics 32(6):601–608, DOI https://doi.org/10.1016/S0021-9290(99)00015-9, URL http://www.sciencedirect.com/science/article/pii/S0021929099000159

Gill B, Cox Jr CS, Aroom KR (2009) Centrifugal pump. US 2009/0317271 A1

Goubergrits L (2006) Numerical modeling of blood damage: current status, challenges and future prospects. Expert review of medical devices 3(5):527–531

Grigioni M, Daniele C, Morbiducci U, D'Avenio G, Di Benedetto G, Barbaro V (2004) The power-law mathematical model for blood damage prediction: analytical developments and physical inconsistencies. Artificial organs 28(5):467–475

Grigioni M, Morbiducci U, D'Avenio G, Di Benedetto G, Del Gaudio C (2005) A novel formulation for blood trauma prediction by a modified power-law mathematical model. Biomechanics and Modeling in Mechanobiology 4(4):249–260

Guest JK, Prévost JH (2006) Topology optimization of creeping fluid flows using a darcy–stokes finite element. International Journal for Numerical Methods in Engineering 66(3):461–484, DOI 10.1002/nme.1560, URL http://dx.doi.org/10.1002/nme.1560

Gurtin ME (1981) An introduction to continuum mechanics, 1st edn. Academic Press, New York

Hasinger SH, Kehrt LG (1963) Investigation of a shear-force pump. Journal of Engineering for Power 85(3):201–206

Hinghofer-Szalkay H, Greenleaf J (1987) Continuous monitoring of blood volume changes in humans. Journal of applied physiology 63(3):1003–1007

Huang H, Ayoub JA (2006) Applicability of the forchheimer equation for non-darcy flow in porous media. In: SPE Annual Technical Conference and Exhibition, Society of Petroleum Engineers

Hunter JD (2007) Matplotlib: A 2d graphics environment. Computing in Science & Engineering 9(3):90–95, DOI 10.1109/MCSE.2007.55

Hyun J, Wang S, Yang S (2014) Topology optimization of the shear thinning non-newtonian fluidic systems for minimizing wall shear stress. Computers & Mathematics with Applications 67(5):1154 – 1170, DOI https://doi.org/10.1016/j.camwa.2013.12.013, URL http://www.sciencedirect.com/science/article/pii/S0898122113007074

Izraelev V, Weiss WJ, Fritz B, Newswanger RK, Paterson EG, Snyder A, Medvitz RB, Cysyk J, Pae WE, Hicks D, et al. (2009) A passively-suspended tesla pump left ventricular assist device. ASAIO journal (American Society for Artificial Internal Organs: 1992) 55(6):556

Jensen KE (2013) Structural optimization of non-newtonian microfluidics. PhD thesis, Technical University of Denmark, phD thesis

Jensen KE, Szabo P, Okkels F (2012) Topology optimizatin of viscoelastic rectifiers. Applied Physics Letters 100(23):234102

Jiang L, Chen S, Sadasivan C, Jiao X (2017) Structural topology optimization for generative design of personalized aneurysm implants: Design, additive manufacturing, and experimental validation. In: 2017 IEEE Healthcare Innovations and Point of Care Technologies (HI-POCT), IEEE, pp 9–13

Joseph DD, Nield DA, Papanicolaou G (1982) Nonlinear equation governing flow in a saturated porous medium. Water Resources Research 18(4):1049–1052, DOI 10.1029/WR018i004p01049, URL https://agupubs.onlinelibrary.wiley.com/doi/abs/10.1029/WR018i004p01049, https://agupubs.onlinelibrary.wiley.com/doi/pdf/10.1029/WR018i004p01049

Kian JdM (2017) Topology optimization method applied to design channels considering non-newtonian fluid flow. Master's thesis, Universidade de São Paulo, URL http://www.teses.usp.br/teses/disponiveis/3/3152/tde-16032017-103709/en.php

Kletschka HD, Rafferty EH (1975) Pumps capable of use as heart pumps and blood pumps. US 3,864,055

Kundu P, Kumar V, Mishra IM (2016) Experimental and numerical investigation of fluid flow hydrodynamics in porous media: Characterization of pre-darcy, darcy and non-darcy flow regimes. Powder Technology 303:278–291

Lai WM, Rubin DH, Krempl E, Rubin D (2009) Introduction to continuum mechanics. Butterworth-Heinemann

Langtangen HP, Logg A (2016) Solving PDEs in Minutes – The FEniCS Tutorial Volume I. URL https://fenicsproject.org/book/

Lasseux D, Valdés-Parada FJ (2017) On the developments of darcy's law to include inertial and slip effects. Comptes Rendus Mécanique 345(9):660 – 669, DOI https://doi.org/10.1016/j.crme.2017.06.005, URL http://www.sciencedirect.com/science/article/pii/S1631072117300979, a century of fluid mechanics: 1870–1970

Lazarov BS, Sigmund O (2010) Filters in topology optimization based on helmholtz-type differential equations. International Journal for Numerical Methods in Engineering 86(6):765–781

Leondes C (2000) Biomechanical Systems: Techniques and Applications, Volume II: Cardiovascular Techniques, 1st edn. Biomechanical Systems: Techniques and Applications, CRC Press

Logg A, Mardal KA, Wells G (2012) Automated solution of differential equations by the finite element method: The FEniCS book, vol 84. Springer Science & Business Media, URL https://fenicsproject.org/book/

Lu P, Lai H, Liu J (2001) A reevaluation and discussion on the threshold limit for hemolysis in a turbulent shear flow. Journal of biomechanics 34(10):1361–1364

Miller GE, Rainer F (1999) Analysis of optimal design configurations for a multiple disk centrifugal blood pump. Artificial Organs 23(6):559–565, DOI 10.1046/j.1525-1594.1999.06403.x, URL https://onlinelibrary.wiley.com/doi/abs/10.1046/j.1525-1594.1999.06403.x, https://onlinelibrary.wiley.com/doi/pdf/10.1046/j.1525-1594.1999.06403.x

Miller GE, Sidhu A, Fink R, Etter BD (1993) Evaluation of a multiple disk centrifugal pump as an artificial ventricle. Artificial Organs 17(7):590–592, DOI 10.1111/j.1525-1594.1993.tb00599.x, URL https://onlinelibrary.wiley.com/doi/abs/10.1111/j.1525-1594.1993.tb00599.x, https://onlinelibrary.wiley.com/doi/pdf/10.1111/j.1525-1594.1993.tb00599.x

Mitoh A, Yano T, Sekine K, Mitamura Y, Okamoto E, Kim DW, Yozu R, Kawada S (2003) Computational fluid dynamics analysis of an intra-cardiac axial flow pump. Artificial Organs 27(1):34–40, DOI 10.1046/j.1525-1594.2003.07190.x, URL https://onlinelibrary.wiley.com/doi/abs/10.1046/j.1525-1594.2003.07190.x, https://onlinelibrary.wiley.com/doi/pdf/10.1046/j.1525-1594.2003.07190.x

Mitusch S, Funke S, Dokken J (2019) dolfin-adjoint 2018.1: automated adjoints for fenics and firedrake. Journal of Open Source Software 4(38):1292, URL https://doi.org/10.21105/joss.01292

Montevecchi F, Inzoli F, Redaelli A, Mammana M (1995) Preliminary design and optimization of an ecc blood pump by means of a parametric approach. Artificial organs 19(7):685–690

Munson BR, Young DF, Okiishi TH (2009) Fundamentals of fluid mechanics, 6th edn. John Wiley & Sons, Inc.

Nam J, Behr M, Pasquali M (2011) Space-time least-squares finite element method for convection-reaction system with transformed variables. Computer methods in applied mechanics and engineering 200(33-36):2562–2576

Nørgaard S, Sigmund O, Lazarov B (2016) Topology optimization of unsteady flow problems using the lattice boltzmann method. J Comput Phys 307(C):291–307, DOI 10.1016/j.jcp.2015.12.023, URL https://doi.org/10.1016/j.jcp.2015.12.023

Olesen LH, Okkels F, Bruus H (2006) A high-level programming-language implementation of topology optimization applied to steady-state navier–stokes flow. International Journal for Numerical Methods in Engineering 65(7):975–1001

Papoutsis-Kiachagias E, Kontoleontos E, Zymaris A, Papadimitriou D, Giannakoglou K (2011) Constrained topology optimization for laminar and turbulent flows, including heat transfer. CIRA, editor, EUROGEN, Evolutionary and Deterministic Methods for Design, Optimization and Control, Capua, Italy

Pauli L, Nam J, Pasquali M, Behr M (2013) Transient stress-based and strain-based hemolysis estimation in a simplified blood pump. International journal for numerical methods in biomedical engineering 29(10):1148–1160

Philippi B, Jin Y (2015) Topology optimization of turbulent fluid flow with a sensitive porosity adjoint method (spam). arXiv:151208445

Pingen G, Maute K (2010) Optimal design for non-newtonian flows using a topology optimization approach. Computers & Mathematics with Applications 59(7):2340–2350

Pinotti M, Rosa ES (1995) Computational prediction of hemolysis in a centrifugal ventricular assist device. Artificial Organs 19(3):267–273

Pratumwal Y, Limtrakarn W, Muengtaweepongsa S, Phakdeesan P, Duangburong S, Eiamaram P, Intharakham K (2017) Whole blood viscosity modeling using power law, casson, and carreau yasuda models integrated with image scanning u-tube viscometer technique. Songklanakarin Journal of Science & Technology 39(5)

Rafferty EH, Kletschka HD (1972) Electrically driven pumps capable of use as heart pumps. US 3,647,324

Rafferty EH, Kletschka HD (1976) Pumping apparatus and process characterized by gentle operation. US 3,957,389

Ramalingom D, Cocquet PH, Bastide A (2018) A new interpolation technique to deal with fluid-porous media interfaces for topology optimization of heat transfer. Computers & Fluids 168:144 – 158, DOI https://doi.org/10.1016/j.compfluid.2018.04.005, URL http://www.sciencedirect.com/science/article/pii/S0045793018301932

Reddy JN, Gartling DK (2010) The finite element method in heat transfer and fluid dynamics, 3rd edn. CRC press

Rey Ladino AF (2004) Numerical simulation of the flow field in a friction-type turbine (tesla turbine). Diploma thesis, Institute of Thermal Powerplants, Vienna University of Technology

Rice W (1991) Tesla turbomachinery

Romero J, Silva E (2014) A topology optimization approach applied to laminar flow machine rotor design. Computer Methods in Applied Mechanics and Engineering 279(Supplement C):268 – 300, DOI https://doi.org/10.1016/j.cma.2014.06.029, URL http://www.sciencedirect.com/science/article/pii/S0045782514002151

Romero JS, Silva ECN (2017) Non-newtonian laminar flow machine rotor design by using topology optimization. Structural and Multidisciplinary Optimization 55(5):1711–1732

Sá LF, Romero JS, Horikawa O, Silva ECN (2018) Topology optimization applied to the development of small scale pump. Structural and Multidisciplinary Optimization 57(5):2045–2059, DOI 10.1007/s00158-018-1966-7, URL https://doi.org/10.1007/s00158-018-1966-7

Sá LFN, Amigo RCR, Novotny AA, Silva ECN (2016) Topological derivatives applied to fluid flow channel design optimization problems. Structural and Multidisciplinary Optimization 54(2):249–264, DOI 10.1007/s00158-016-1399-0, URL https://doi.org/10.1007/s00158-016-1399-0

Sabersky RH, Acosta AJ, Hauptmann EG, Gates EM (1971) Fluid flow: a first course in fluid mechanics, vol 299. Macmillan

Sastry S, Kadambi JR, Sankovic JM, Izraelev V (2006) Study of flow field in an advanced bladeless rotary blood pump using particle image velocimetry. Lisbon, Portugal

Sato Y, Yaji K, Izui K, Yamada T, Nishiwaki S (2018) An optimum design method for a thermal-fluid device incorporating multiobjective topology optimization with an adaptive weighting scheme. Journal of Mechanical Design 140(3):031402

Sokolowski J, Zochowski A (1999) On the topological derivative in shape optimization. SIAM journal on control and optimization 37(4):1251–1272

Song X, Throckmorton AL, Wood HG, Antaki JF, Olsen DB (2003) Computational fluid dynamics prediction of blood damage in a centrifugal pump. Artificial Organs 27(10):938–941, DOI 10.1046/j.1525-1594.2003.00026.x, URL https://onlinelibrary.wiley.com/doi/abs/10.1046/j.1525-1594.2003.00026.x, https://onlinelibrary.wiley.com/doi/pdf/10.1046/j.1525-1594.2003.00026.x

Song XG, Wang L, Baek SH, Park YC (2009) Multidisciplinary optimization of a butterfly valve. ISA transactions 48(3):370–377

Sonntag RE, Borgnakke C (2013) Fundamentals of Thermodynamics, 8th edn. Wiley

Taskin ME, Fraser KH, Zhang T, Wu C, Griffith BP, Wu ZJ (2012) Evaluation of eulerian and lagrangian models for hemolysis estimation. ASAIO journal 58(4):363–372

Tesch K (2013) On invariants of fluid mechanics tensors. Task Quarterly 17(3-4):228–230

Vafai K (2005) Handbook of porous media, 2nd edn. Crc Press

Wächter A, Biegler LT (2006) On the implementation of an interior-point filter line-search algorithm for large-scale nonlinear programming. Mathematical programming 106(1):25–57

Wang L, Torres A, Xiang L, Fei X, Naido A, Wu W (2015) A technical review on shale gas production and unconventional reservoirs modeling. Natural Resources 6(03):141

Ward JC (1964) Turbulent flow in porous media. Journal of the Hydraulics Division 90(5):1–12

White FM (2009) Fluid Mechanics, 7th edn. McGraw-Hill, 2011

Wiker N, Klarbring A, Borrvall T (2007) Topology optimization of regions of darcy and stokes flow. International journal for numerical methods in engineering 69(7):1374–1404

Wu J (2007) Letter to the editor: A possible major mistake in the paper entitled "collected nondimensional performance of rotary dynamic blood pump": Smith wa, allaire p, antaki j, butler kc, kerkhoffs w, kink t, loree h, reul h. asaio journal 50: 25–32, 2004. Asaio Journal 53(2):255–256

Wu J, Antaki JF, Snyder TA, Wagner WR, Borovetz HS, Paden BE (2005) Design optimization of blood shearing instrument by computational fluid dynamics. Artificial organs 29(6):482–489

Yano T, Sekine K, Mitoh A, Mitamura Y, Okamoto E, Kim DW, Nishimura I, Murabayashi S, Yozu R (2003) An estimation method of hemolysis within an axial flow blood pump by computational fluid dynamics analysis. Artificial organs 27(10):920–925

Yeleswarapu KK, Antaki JF, Kameneva MV, Rajagopal KR (1995) A mathematical model for shear-induced hemolysis. Artificial Organs 19(7):576–582

Yoon GH (2016) Topology optimization for turbulent flow with spalart–allmaras model. Computer Methods in Applied Mechanics and Engineering 303:288 – 311, DOI https://doi.org/10.1016/j.cma.2016.01.014, URL http://www.sciencedirect.com/science/article/pii/S004578251630007X

Yoon GH (2020) Topology optimization method with finite elements based on the k-ε turbulence model. Computer Methods in Applied Mechanics and Engineering 361:112784, DOI https://doi.org/10.1016/j.cma.2019.112784, URL http://www.sciencedirect.com/science/article/pii/S0045782519306760

Yu H (2015) Flow design optimization of blood pumps considering hemolysis. PhD thesis, Magdeburg, Universität, Diss., 2015

Zauderer E (1989) Partial differential equations of applied mathematics, 2nd edn. John Wiley & Sons

Zhang B, Liu X (2015) Topology optimization study of arterial bypass configurations using the level set method. Struct Multidiscip Optim 51(3):773–798, DOI 10.1007/s00158-014-1175-y, URL http://dx.doi.org/10.1007/s00158-014-1175-y

Zhang B, Liu X, Sun J (2016) Topology optimization design of non-newtonian roller-type viscous micropumps. Structural and Multidisciplinary Optimization 53(3):409–424

Zhang T, Taskin ME, Fang HB, Pampori A, Jarvik R, Griffith BP, Wu ZJ (2011) Study of flow-induced hemolysis using novel couette-type blood-shearing devices. Artificial organs 35(12):1180–1186

Zhou S, Li Q (2008) A variationals level set method for the topology optimization of steady-state navier–stokes flow. Journal of Computational Physics 227(24):10178–10195